Distinct molecular programs regulate synapse specificity in cortical inhibitory circuits

Emilia Favuzzi[1,2,3,4], Rubén Deogracias[1,2,3,4], André Marques-Smith[1,2], Patricia Maeso[1,2,3], Julie Jezequel[1,2], David Exposito-Alonso[1,2], Maddalena Balia[1,2], Tim Kroon[1,2], Antonio J. Hinojosa[1,2,3], Elisa F. Maraver[1,2] & Beatriz Rico[1,2,3,*]

[1]Centre for Developmental Neurobiology, Institute of Psychiatry, Psychology and Neuroscience, King's College London, London SE1 1UL, United Kingdom

[2]MRC Centre for Neurodevelopmental Disorders, King's College London, London SE1 1UL, United Kingdom

[3]Instituto de Neurociencias, Consejo Superior de Investigaciones Científicas & Universidad Miguel Hernández, Sant Joan d'Alacant 03550, Spain

[4]These authors contribute equally

*Correspondence should be addressed to B.R. (beatriz.rico@kcl.ac.uk)

One sentence summary: **Connection target specificity in inhibitory neurons is conferred by cell-specific expression of synaptic molecules.**

ABSTRACT

How neuronal connections are established and organized in functional networks determines brain function. In the mammalian cerebral cortex, different classes of GABAergic interneurons exhibit specific connectivity patterns that underlie their ability to shape temporal dynamics and information processing. Much progress has been made parsing interneuron diversity, yet the molecular mechanisms by which interneuron-specific connectivity motifs emerge remain unclear. Here we investigate transcriptional dynamics in different classes of interneurons during the formation of cortical inhibitory circuits in mouse. We found that whether interneurons synapse on the dendrites, soma or axon initial segment of pyramidal cells is determined by synaptic molecules that are expressed in a subtype-specific manner. Thus cell-specific molecular programs that unfold during early postnatal development underlie the connectivity patterns of cortical interneurons.

MAIN TEXT

Different classes of neurons connect with exquisite specificity to form neuronal circuitries. Brain wiring is most complex in the cerebral cortex, that includes excitatory pyramidal cells and inhibitory GABAergic interneurons, of which over two dozen types have been identified (*1*). Different types of interneuron target distinct subcellular compartments in pyramidal cells. For example, somatostatin-expressing (SST+) interneurons primarily contact the dendrites of pyramidal cells, whereas parvalbumin-expressing (PV+) basket cells make synapses on neuronal somata and proximal dendrites. Chandelier cells, instead, innervate the axonal initial segment

(AIS) of pyramidal neurons (*2*). Compartment-specific inhibitory control confers advanced computational capabilities to neurons (*3*, *4*). Here we study in mouse the mechanisms regulating compartment-specific wiring of interneuron outputs in cortical microcircuits. Molecular signatures identify types of interneuron in the adult mouse cerebral cortex (*1*, *5*, *6*). However, cell type-specific transcriptional differences may drive subcellular patterns of inhibitory connectivity and may be restricted to early postnatal development, when synapses are formed.

To identify cell type-specific molecular programs controlling the subcellular connectivity of SST+, PV+ basket and chandelier interneurons, we first analyzed the temporal dynamics of inhibitory synapse formation for each of these populations (fig. S1). Postnatal day (P) 10 marks the initial surge of synaptogenesis for all three classes of interneuron (fig. S1). These results provided us with a developmental time window for searching gene expression differences underlying the establishment of type-specific interneuron connectivity.

To identify genes that are differentially expressed between different classes of interneurons during inhibitory synapse formation, we used fluorescence-activated cell sorting to isolate interneurons from genetically modified mice in which dendritic-, somatic- and AIS-targeting GABAergic interneurons are enriched and labeled (table S1) (*7–12*). We isolated interneurons both prior (P5/P8) and during peak (P10) synaptogenesis. To ensure cell type and developmental stage specificity, we also isolated several control populations: interneurons at P0, pyramidal neurons at the peak of glutamatergic synaptogenesis (P12, (*13*)) and oligodendrocytes at P10 (table S1 and S2). We then performed RNA-sequencing (RNAseq) and whole-transcriptome analyses on each of these cell populations to identify the molecular programs that distinguish different interneuron types between P5 and P10 (Fig. 1A and fig. S2A;

https://devneuro.org/cdn/gene_tool_1.php). Gene expression profiles from different types of interneuron showed similar patterns of distribution, consistency across biological replicates, accurate segregation for each cell type and suitability of the selected developmental time points (fig. S2).

To query which molecules regulate interneuron synapse specificity, we first identified differentially expressed (DE) genes among distinct types of interneuron during the initial period of synaptogenesis (Fig. 1). Differential expression analysis revealed type-specific gene expression at P10 (Fig. 1B and fig. S3C). Gene Ontology (GO) analysis revealed that the most enriched genes belong to synaptic, nearby membrane compartments and included processes that contribute to synaptogenesis (Fig. 1C and D, and fig. S3). Notably, comparison of our dataset with recent scRNA-seq studies from the adult mouse cortex unveiled that many genes that are type-specific during development are not detected as such at later stages (fig. S4-S6). Altogether, these analyses indicate that distinct transcriptomic profiles emerge in developing interneurons and that a large proportion of the type-specific signatures are restricted to the time of synapse assembly (P5-P10).

To single out genes with the highest degree of type and stage specificity, we ranked DE genes using a specificity ratio ((*14*), see Methods). Our analyses (i) indicate that different interneurons acquire distinct molecular signatures while they first establish synaptic contacts (Fig. 1E) and (ii) revealed several gene subsets potentially involved in the establishment of distinct inhibitory motifs (dendrite-, soma- and AIS-targeting) in the developing cerebral cortex (Fig. 2A, S7 and table S3 and S4). Indeed, our data showed that distinct members of synaptic protein families are often differentially utilized by interneuron subclasses during development (Fig. 2B and Fig. S8). Focusing on genes that had a putative or established synaptic

function (Fig. 2A and B), we identified and validated those that exhibited the highest specificity (Fig. 2, S9 and S10). Such validation yielded three candidate genes that we further studied to demonstrate that inhibitory synapse specificity is conferred by cell-specific expression of synaptic molecules. The leading candidate for regulating dendrite-targeting inhibitory synapses was *Cbln4*, a member of the C1q family that is a bidirectional synaptic organizer (*15*, *16*). Leucine rich repeat LGI family member 2 (*Lgi2*), that belongs to a protein family involved in synapse maturation (*17*), emerged as a promising candidate to regulate the development of perisomatic inhibitory synapses. Finally, *Fgf13*, which encodes an intracellular protein with multiple functions including a microtubule stabilizing role (*18–21*), was our candidate for AIS-targeting chandelier synapses. Supporting our hypothesis that these genes aid inhibitory synapse development, *Lgi2* and *Fgf13* dysfunction has been linked to disorders characterized by disrupted excitatory/inhibitory balance (*22–24*).

We examined mRNA or protein expression for our candidate genes and confirmed that their expression increased during the second postnatal week (Fig 2C). We also confirmed that in the cerebral cortex, both at P10 and P30, *Cbln4*, *Lgi2* and *Fgf13* are enriched in SST+, PV+ and chandelier cells, respectively (Fig. 2D and E, fig. S10 and fig. S11). Examining the proportion of interneurons of each type that express our candidate genes, one can see that *Cbln4* and *Fgf13* are ubiquitously expressed by all SST+ interneurons and chandelier cells, respectively, whereas *Lgi2* is confined to a subpopulation of PV+ basket cells (Fig. 2D and E and fig. S10).

To investigate the role of *Cbln4*, *Lgi2* and *Fgf13* in the development of different types of GABAergic synapses, we used a hybrid conditional gene knock-down strategy based on cell-type specific Cre-driver lines combined with adeno-associated viral vectors (AAV) and performed cell type-specific loss-of-function experiments in

vivo (*25*). In brief, we engineered Cre-dependent conditional constructs expressing miR-based short-hairpin RNAs against candidate genes (*shCbln4*, *shLgi2*, *shFgf13*) and controls (*shLacZ* and *shGfp*) in which recombination was reported by mCherry (fig. S12A). We confirmed the effectiveness of our constructs in downregulating *Cbln4*, *Lgi2*, *Fgf13* expression (fig. S12, B to E).

Compared to controls, cell-specific downregulation of *Cbln4* in SST+ cells, *Lgi2* in PV+ basket cells and *Fgf13* in chandelier cells led to a decrease in the density of presynaptic inputs (mCherry+) that these interneurons make onto the corresponding subcellular postsynaptic compartments of pyramidal cells (Fig. 3 and fig. S13). We observed that *Fgf13*-deficient chandelier cells also showed axonal disorganization (fig. S14, A to D), which was instead not found in SST+ or PV+ basket cells upon downregulation of *Cbln4* and *Lgi2*, respectively (fig. S15). The axonal phenotype of *Fgf13*-deficient chandelier cells may contribute to their decreased innervation of the AIS. Nevertheless, the reduced density of chandelier synaptic boutons persisted when *Fgf13* was downregulated after P14 when the axonal phenotype was, instead, not observed (fig. S14, E to H), suggesting two different functions of the protein.

Control as well as rescue experiments showed that our phenotypes are explained by specific downregulation of the target genes rather than off-target effects and did not include an altered interneuron density (figs. S16, S17 and S18). Moreover, GluD1 and ADAM22 – CBLN4 and LGI2 putative trans-synaptic partners (*23*, *26*) – are located at the SST+ and PV+ synapses, respectively (fig. S19).

Altogether, these experiments revealed that *Cbln4*, *Lgi2* and *Fgf13* are required for the development of dendrite-, soma- and AIS-targeting synapses made by SST+ interneurons, PV+ basket cells and chandelier cells, respectively. Such one to one matching of molecules to cell types uncovers that the connectivity patterns of cortical

interneurons rely on synaptic protein repertoires that are selective for each type of interneuron. Notably, Cre-dependent knockdown of *Pcdh18* – another developmentally regulated molecule specifically expressed in SST+ cells (Fig. 2A and S20, A to F) – led to an increase in the density of SST+ dendritic synapses (Fig. S20, G to J). Thus, our screening is a valuable resource for identifying molecules regulating diverse aspects of inhibitory synapse assembly and specificity.

The subcellular localization of presynapses defines the efferent specificity in each type of interneuron. We, therefore, asked whether the identified cell-specific synaptic molecules can regulate synapse formation independently of the subcellular location of presynaptic terminals. To this end, we focused on *Cbln4* because C1q family proteins can induce synapse formation (*16*). We first validated the synaptic deficits observed following loss of Cbln4 in SST+ interneurons. Specifically, we injected AAV viruses expressing Channelrhodopsin-2 (Chronos) following Cre-mediated recombination along with control or *shCbln4* vectors (Fig. 4A). *Cbln4* downregulation in SST+ interneurons did not affect their spiking output or membrane properties in response to photostimulation (Fig. S21). We recorded from pyramidal neurons and stimulated ChR2+ SST cells with wide-field illumination of increasing intensity, finding that the peak amplitude of optogenetically-evoked inhibitory postsynaptic currents (IPSCs) was reduced in knockdown animals versus controls (Fig. 4B to D). Minimal intensity stimulation experiments revealed a decrease in IPSC amplitude in cells recorded from knockdown animals (Fig. 4D). These findings suggest a decrease in synaptic weights for SST outputs to pyramidal cells, offering a functional correlate consistent with the structural synaptic deficits caused by downregulation of *Cbln4* in SST+ cells (Fig. 3B and C).

Next, we investigated whether *Cbln4* is sufficient to trigger the formation of domain-restricted synapses. We observed that overexpression of a HA-tagged CBLN4 in SST+ interneurons leads to an increase in dendritic inhibitory synapses (Fig. 4E to F). In contrast, ectopic expression of CBLN4 in PV+ basket cells or chandelier cells did not promote synapse formation on the soma or AIS of pyramidal cells but caused a specific increase in PV+ dendritic synapses (Fig. 4G to L and fig. S22). These results indicate that *Cbln4* expression does not trigger generic formation of all inhibitory synapses. Rather, *Cbln4* promotes the formation of GABAergic synapses onto the dendrites of pyramidal cells, a feature that is distinctive of SST+ interneurons.

Our study reveals transcriptional dynamics for different classes of interneurons from P5 to P10 in postnatal development of the mouse, when inhibitory circuits are established in the cerebral cortex. Although post-transcriptional processes (e.g. local translation) are likely to play an additional role, our results describe a relationship between cortical interneuron development and diversity. We demonstrate that different classes of interneurons rely on largely non-overlapping molecular programs for the establishment of distinct types of inhibitory synapses. In particular, we show that three molecules — CBLN4, LGI2 and FGF13— regulate the development of SST+, PV+ basket and chandelier synapses, respectively. Specifically, CBLN4 is able to promote the assembly of dendritic but not somatic or axo-axonic inhibitory synapses. These results demonstrate how the cell-specific expression of synaptic molecules together with their ability to promote compartment-specific synapse formation critically contributes to the specific wiring of the inhibitory circuits.

Insight into the organizing principles of cortical inhibitory circuits will help deciphering neurodevelopmental disorders linked to inhibitory circuit dysfunction

(*24*, *27*). Much progress has been made towards understanding interneuron diversity during embryonic development or in the adult cortex (*1*, *6*, *28–30*). Our work reveals that selective type-specific genetic programs emerge during postnatal development in cortical interneurons to support the exquisite precision of inhibitory connections, thereby assembling inhibitory circuits. Since some of these genes continue to be expressed in mature cortical interneurons (*1*, *5*, *6*), it is conceivable that they also contribute to the maintenance and plasticity of specific inhibitory circuitries.
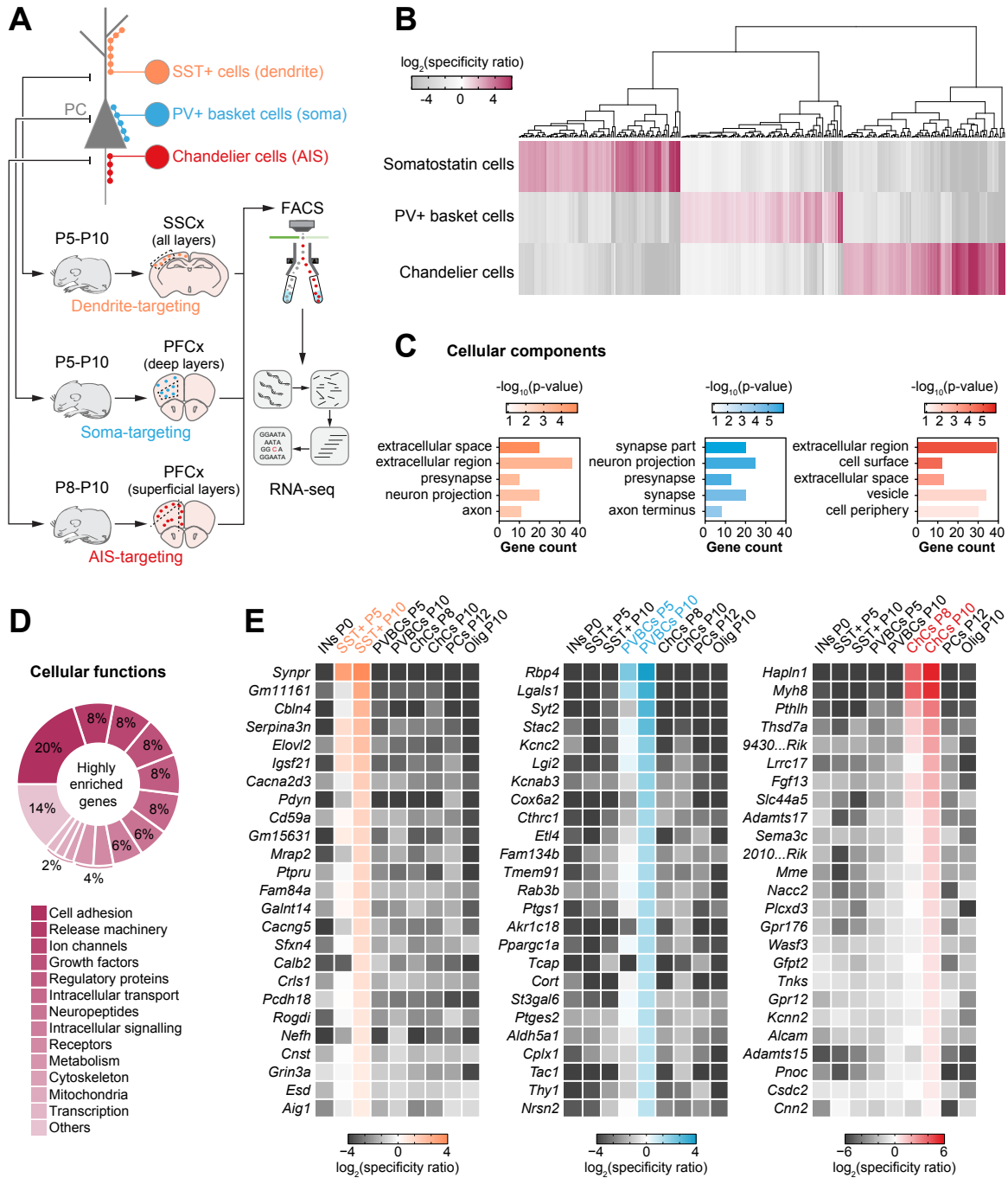
ACKNOWLEDGMENTS

SUPPLEMENTARY MATERIALS

Materials and Methods

Figs. S1 to S22

Tables S1 to S4

FIGURES

Fig. 1. Identification of cell type-specific molecular programs for interneuron postnatal development.

Fig. 2. Expression of subtype-specific synaptic genes

Fig. 3. Genetic specification of interneuron synapse formation.

A LED
AAV-FLEX-Chronos-GFP
AAV-DIO-shCbln4-mCherry

Sst^{Cre/+}

B

C 500pA / 100 ms

D shControl / shCbln4
Minimal IPSC Amplitude (pA)
*

IPSC amplitude (pA) vs Irradiance (log₂ mW/mm²)
***

E mCherry GAD65 Gephyrin
Control
+Cbln4

AAV-DIO-Cbln4 -mCherry
Sst^{Cre/+}

F Control / Cbln4-HA
Synapses/µm³ axon
***

G Control / +Cbln4
mCherry Syt2 GFP (pyramidal cells)

AAV-DIO-Cbln4 -mCherry
PV^{Cre/+}

H Control / Cbln4-HA
Syt2+mCherry+ boutons/µm² soma
ns

I Control / +Cbln4
mCherry Syt2 GFP

AAV-DIO-Cbln4 -mCherry
PV^{Cre/+}

J Control / Cbln4-HA
Syt2+mCherry+ boutons/µm² dendrite
*

K Control / +Cbln4
mCherry AnkG

AAV-DIO-Cbln4 -mCherry
Nkx2-1^{CreER/+}

L Control / Cbln4-HA
Chandelier boutons/µm² AIS
ns

Fig. 4. Synaptic function and target specificity for SST+ population

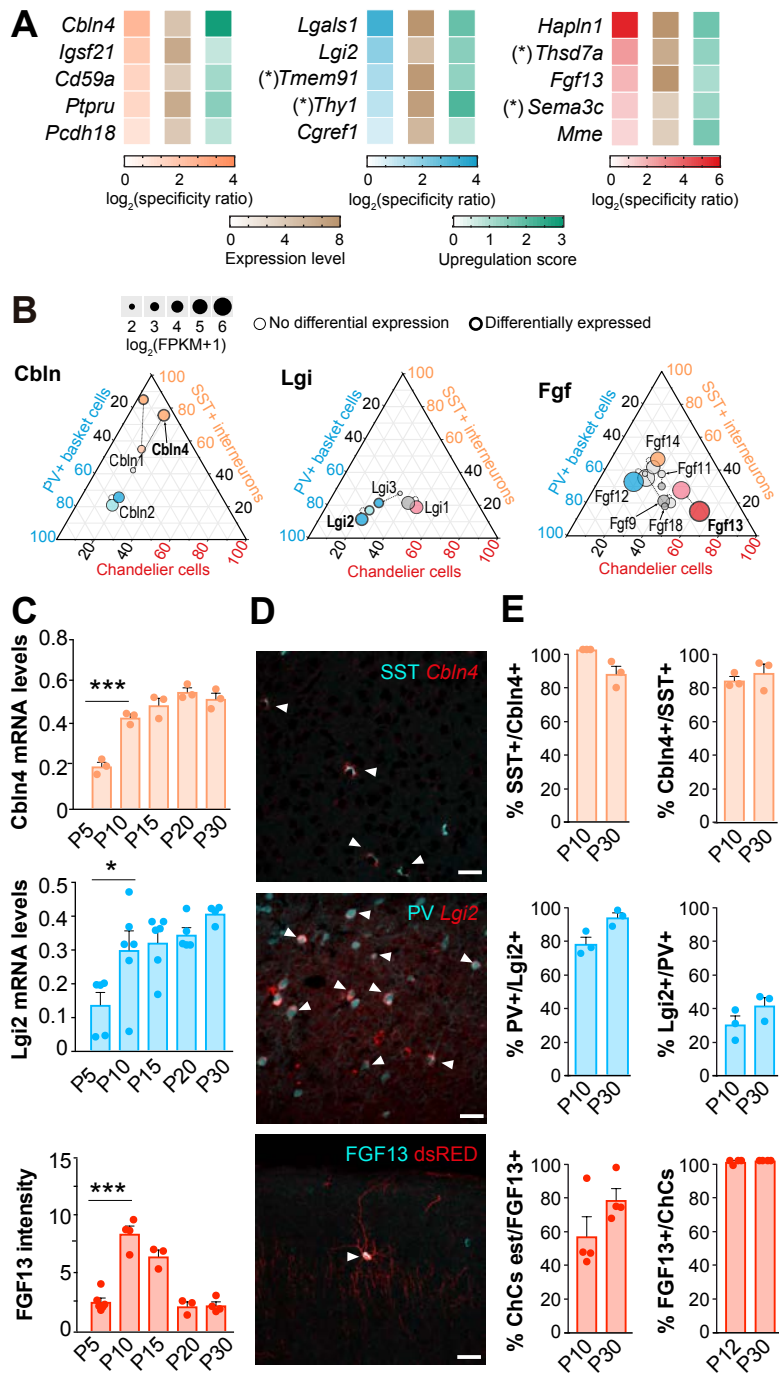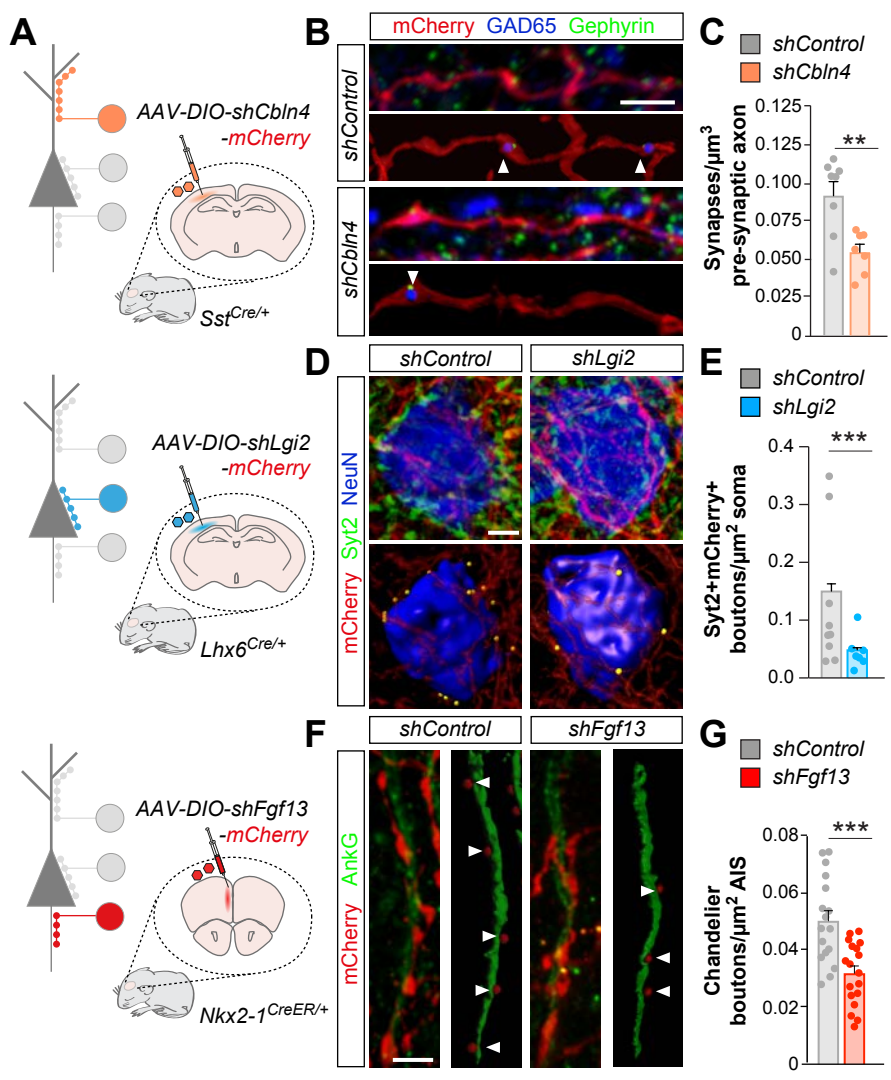# FIGURE LEGENDS

Fig. 1. Identification of cell type-specific molecular programs for interneurons postnatal development. (**A**) Schematic of experimental workflow. (**B**) Heatmap showing P10 interneuron-subtype enriched genes. (**C** and **D**) GO analysis using P10 subtype-specific genes: terms associated with synapses (**C**, see fig. S3) and cellular functions (**D**). (**E**) Heatmaps showing the top 25 differentially expressed genes exhibiting the highest degree of subtype and stage specificity.

Fig. 2. Expression of subtype-specific synaptic genes. (**A**) Top 5 candidate subtype-specific 'synaptic' genes. Asterisk: synaptic function by similarity. (**B**) Ternary diagrams showing subtype and time differences in expression (light colors P5, darker P10, grey not enriched). (**C**) Developmental expression of *Cbln4* and *Lgi2* in the somatosensory cortex (qPCR, *Lgi2* values are x10^{-5}) and *Fgf13* (IHC, fluorescence intensity in arbitrary units x10^{-2}) in layer II-III of prefrontal cortex (n ≥ 3 mice for each stage). One-Way ANOVA (*Cbln4* and FGF13) or Kruskal-Wallis test (*Lgi2*) and Tukey's or Dunn's multiple comparisons test. ***p<0.001, *p<0.05; significance shown only for P5-P10 comparisons. (**D**) Expression of *Cbln4*, *Lgi2* and FGF13 in SST+, PV+ basket and chandelier cells, respectively. Scale bars equal to 20 μm. (**E**) Specificity of *Cbln4*, *Lgi2* and FGF13 expression (left column). Fraction of SST+, PV+ basket and chandelier cells expressing *Cbln4*, *Lgi2* and FGF13 (right column). "ChCs est", estimated number of chandelier cells (Fig S4, E to G). Data are mean ± SEM.

Fig. 3. Genetic specification of interneuron synapse formation. (**A**) Schematic of AAV injections. (**B** to **C**) Representative image, Imaris reconstruction and density of GAD65+ boutons inside mCherry+ axons of SST+ cells infected with control (n = 8 mice) or *shCbln4*-expressing viruses (n = 7 mice) contacting Gephyrin+ clusters in layer I. **p<0.01, Student t-test. (**D** to **E**) Representative images, Imaris reconstruction and density of mCherry+Syt2+ synapses made by PV+ basket cells infected with control (n = 5 mice) or *shLgi2*-expressing virus (n = 6 mice). **p<0.01, Student t-test. (**F** to **G**) Representative images, Imaris reconstruction and density of mCherry+ synapses made by chandelier cells induced with Tamoxifen and infected with control (n = 18 cells from 3 mice) or *shFgf13*-expressing viruses (n = 18 cells from 5 mice). ***p<0.001, Student t-test. Scale bars equal 1 μm. Data are mean ± SEM.

Fig. 4. Synaptic function and target specificity for SST population. (**A**) Schematic of experimental paradigm (n= 18 cells from 9 and 7 mice for control and *shCbln4*-expressing viruses, respectively). (**B**) IPSC peak amplitude as a function of irradiance, ***p<0.001, Two-Way ANOVA. (**C**) Representative IPSC traces. (**D**) IPSC amplitude under minimal intensity, *p<0.05, Mann-Whitney test. (**E** to **F**) Representative image, Imaris reconstruction and density of GAD65+ boutons inside mCherry+ axons of SST+ cells infected with control (n = 9 mice) or *Cbln4*-HA-expressing virus (n = 8 mice) contacting Gephyrin+ clusters in layer I. ***p<0.001, Mann-Whitney test. (**G** to **J**) Representative images, Imaris reconstruction and density of mCherry+Syt2+ synapses made onto pyramidal cell soma or dendrites by PV+ basket cells infected with control (n = 5 mice) or *Cbln4*-HA-expressing virus (n = 5 mice). ns, Student t-test (H), * p<0.05, Mann-Whitney test (J). (**K** to **L**) Representative images, Imaris reconstruction and density of mCherry+ synapses made by chandelier cells induced with Tamoxifen and infected with control (n = 12 cells from 3 mice) or *Cbln4*-HA-expressing virus (n = 17 cells from 5 mice). ns, Student t-test. Scale bars equal 1 μm. Data are mean ± SEM.

REFERENCES AND NOTES

1. B. Tasic *et al*., *Nat Neurosci*. **19**, 335–346 (2016).
2. R. Tremblay, S. Lee, B. Rudy, *Neuron* **91**, 260–292 (2016).
3. F. Pouille, M. Scanziani, *Science* **293**, 1159–1163 (2001).
4. X. J. Wang, J. Tegnér, C. Constantinidis, P. S. Goldman-Rakic, *Proc Natl Acad Sci U S A*. **101**, 1368–1373 (2004).
5. A. Zeisel *et al*., *Science* **347**, 1138–1142 (2015).
6. A. Paul *et al*., *Cell* **171**, 522–539.e20 (2017).
7. B. Chattopadhyaya *et al*., *J Neurosci*. **24**, 9598–9611 (2004).
8. A. A. Oliva, M. Jiang, T. Lam, K. L. Smith, J. W. Swann, *J Neurosci*. **20**, 3354–3368 (2000).
9. H. Taniguchi, J. Lu, Z. J. Huang, *Science* **339**, 70–74 (2013).
10. K. Sugino *et al*., *Nat Neurosci*. **9**, 99–107 (2006).
11. X. Xu, E. M. Callaway, *J Neurosci*. **29**, 70–85 (2009).
12. J.-M. Yang *et al*., *J Neurosci*. **33**, 19724–19733 (2013).
13. A. Hinojosa, R. Deogracias, B. Rico, *Cell Rep*. (2018).
14. S. Siegert *et al*., *Nat Neurosci*. **15**, 487–95, S1 (2012).
15. M. Yuzaki, *Eur J Neurosci*. **32**, 191–197 (2010).
16. M. Yuzaki, *Curr Opin Neurobiol*. **45**, 9–15 (2017).
17. K. L. Lovero, Y. Fukata, A. J. Granger, M. Fukata, R. A. Nicoll, *Proc Natl Acad Sci U S A*. **112**, E4129-37 (2015).
18. M. Goldfarb *et al*., *Neuron* **55**, 449–463 (2007).
19. J. L. Pablo, C. Wang, M. M. Presby, G. S. Pitt, *Proc Natl Acad Sci U S A*. **113**, E2665-74 (2016).
20. L. Yang *et al*., *Neuron* **93**, 806–821.e9 (2017).
21. Q.-F. Wu *et al*., *Cell* **149**, 1549–1564 (2012).
22. R. S. Puranam *et al*., *J Neurosci*. **35**, 8866–8881 (2015).
23. E. H. Seppälä *et al*., *PLoS Genet*. **7**, e1002194 (2011).
24. O. Marín, *Nat Med*. **22**, 1229–1238 (2016).
25. E. Favuzzi *et al*., *Neuron* **95**, 639–655.e10 (2017).
26. M. Yasumura *et al*., *J Neurochem*. **121**, 705–716 (2012).
27. J. T. Paz, J. R. Huguenard, *Nat Neurosci*. **18**, 351–359 (2015).
28. X. Jiang *et al*., *Science* **350**, aac9462 (2015).
29. D. Mi *et al*., *Science* 360:81-85 (2018).
30. C. Mayer *et al*., *Nature* 555:457-462 (2018).

Materials and Methods

<u>Mice</u>

$PV^{Cre/+}$ (*31*), $PLP^{GFP/+}$ (*32*), $Nkx2$-$1^{Cre/+}$ (*33*), Nex^{Cre} (*34*), $Sst^{Cre/+}$ (Jackson Laboratories #13044), *Ai9* (Jackson Laboratories #7909) and *RCE* (Jackson Laboratories #32037) were maintained in a C57BL/6 background (Charles River Laboratories); *GIN* mice (Jackson Laboratories #003718) were maintained in an FVB/NJ background, *G42* mice (Jackson Laboratories #007677) were maintained in a CB6F1/J background and $Nkx2$-$1^{CreER/+}$ mice (*9*) were maintained in a 129S2/SV background. Animals were maintained under standard, temperature controlled, laboratory conditions. Mice were kept on a 12:12 light/dark cycle and received water and food *ad libitum*. Animal procedures were approved by ethical committees (IN-CSIC and King's College London) and conducted in accordance with Spanish and European regulations and Home Office personal and project licenses under the UK Animals (Scientific Procedures) 1986 Act.

<u>Choice of transgenic lines, regions and postnatal stages for RNA-seq</u>

We selected specific subpopulations of GABAergic neurons that were fluorescently labeled and highly and/or exclusively represented in particular areas: dendritic-targeting interneurons (*GIN* strain, somatosensory cortex- mostly Martinotti cells (*8*, *11*)), somatic-targeting interneurons (*G42* strain, prefrontal lower layers, PV+ basket cells (*7*, *11*)) and AIS-targeting interneurons (*Nx2.1CreERT2;Ai9* strain, upper layers- mostly chandelier cells upon early postnatal tamoxifen inductions (P2), (*9*) Fig. 1, Table 1). It is important to mention that, because P2 tamoxifen inductions label the very last temporal cohort of chandelier cells, several of these cells are still migrating at P5 (data not shown). To avoid isolating migrating chandelier cells that would "contaminate" our transcriptome data with genes involved in chandelier cell migration rather than synapse formation, we decided to sort chandelier cells at P8 and P10, instead of P5 and P10 (Table 1). Note that it is not possible to unequivocally identify chandelier cells by morphology before P12 (i.e. at P10). Since no chandelier cell is labeled in the lower layers of the *G42* prefrontal cortex (*12*, *35*), this region has the additional advantage of restricting GFP expression exclusively to the PV+ basket cell population, as it also excludes other PV+ cells such as bi-stratified cells (*12*). In contrast, $Nkx2$-$1^{CreER/+}$ subpopulation, although enriched in chandelier cells, still labeled a small fraction of non-chandelier cells. Since knowing the identity of these cells was critical to ensure a correct interpretation of the chandelier cell transcriptome data, we crossed $Nkx2$-$1^{CreER/+}$ mice with the *Ai9* reporter line and colocalized Tomato+ cells with markers (data not shown). At P30, the majority of Tomato+ cells in the upper layers of the PFC were chandelier cells, both PV+ and PV-. We also found a 16% of PV+ basket cells. The remaining 10% were mostly Reelin-expressing neurogliaform (RELN+SST-) interneurons derived from the preoptic area (POA) (*36*) and oligodendrocytes. To exclude genes that might not be playing a specific role in synapse formation, we obtained additional profiles using different reporter lines (Table 1). For example, for genes that might be involved in earlier stages of development, we used $Nkx2$-$1^{Cre/+}$;*RCE* at P0. For genes participating in general process of synapse formation, we use a pyramidal cell reporter line ($Nex^{Cre/+}$;*RCE*) at P12, when we observed the first increase in excitatory synapse formation (*37*). Finally, to remove genes that were expressed in $Nkx2$-$1^{CreER/+}$;Ai9 oligodendrocytes and not chandelier cells we

used $PLP^{GFP/+}$ mice at P10. Since GIN is a transgenic mouse line, the full population of cells labeled by GFP cannot be assumed and has to be characterized. All studies that have used the GIN mice to analyze somatostatin cells have been performed in the somatosensory cortex. We, therefore, reasoned that it was the most accurate area to ensure pure sorting of somatostatin interneurons (8, 11, 38, 39). Moreover, recent work showed that interneurons subtypes from different cortical areas (including SST+ cells) are transcriptionally similar (40).

Background and regional differences

The mouse lines used for RNA-seq have a different background. To confirm that we could reproduce our findings in a homogenous background, all validations of the specific expression (in situ hybridization and immunohistochemistry) as well as the developmental upregulation (qPCR) of *Cbln4*, *Lgi2* and *Fgf13* (and *Pcdh18*) were consistently done in a C57BL/6 background. Moreover, downregulation, rescue and overexpression experiments were also consistently performed in a C57BL/6 background. Regarding the regional differences, as reported above, recent work showed that interneurons subtypes from different cortical areas are transcriptionally similar (40).

Tissue dissociation and FACS

To isolate individual cells, we euthanized the corresponding transgenic mice (Table 1), extracted the brain and microdissected the region of interest in cold pH 7.3 dissociation media containing 14 mM $MgCl_2$, 2 mM HEPES (Invitrogen 15630-106), 0.2 mM NaOH (Sigma S0899), 90 mM Na_2SO_4 (Sigma S6547), 30 mM K_2SO_4 (Sigma P9458), 3.6 mg/mL D-(+)-Glucose (Sigma G6152), 0.8 mM kynurenic acid (Sigma K3375), 50 μM AP-V (Sigma A5282), 50 U/mL penicillin/streptomycin (Thermo Fisher 15140122). Brain regions were identified using histological landmarks (e.g. size and shape of the corpus callosum, big blood vessels, etc.). Regarding the specific layers, the experimenters were trained in the dissection for several weeks as follows: first, upper layers containing tdTomato+ cells or lower layers containing GFP+ cells were dissected under a fluorescent microscope. In the second phase of the training, the distribution of tdTomato+/GFP+ cells under a fluorescent microscope before dissection was used to identify histological landmarks. The accuracy of the dissection was then verified under a fluorescent microscope. Third, the experimenters would perform the layer dissection and then verify the outcome under a fluorescent microscope. To generate single-cell suspensions, 1 mm^3 tissue pieces from 1-3 brains were pooled and enzymatically digested in dissociation medium containing 0.16 mg/mL cysteine (Sigma C9768), 7 U/mL Papain (Sigma P3125), 0.1 mg/mL DNase (Sigma 10104159001) at 37˚ C for 30 minutes. Papain digestion was then blocked with dissociation medium containing 0.1 mg/mL ovomucoid (Sigma, St. Louis, MO T2011) and 0.1 mg/mL bovine serum albumin (BSA, Sigma A4161) for 1 minute at room temperature. Neurons were mechanically dissociated to create a single cell suspension in iced OptiMEM solution containing 3.6 mg/mL D-(+)-Glucose, 4 mM $MgCl_2$, 0.4 mM kynurenic acid, 25 μM AP-V, 0.04 mg/mL DNase diluted in OptiMEM medium (Thermo Fisher, 31985). Cells were centrifuged at 120 g for 5 minutes at 4˚ C, resuspended in 150-300 μL of fresh complemented OptiMEM and passed through a 40 μm cell strainer. Fluorescently labeled individual cells were then purified from the suspension by fluorescence-activated cell sorting (FACS) using a BD

FACSAria III cytometer. Cells from 1-3 consecutive experiments were collected in 350 µl of RLT buffer (RNeasy Lysis buffer, QIAGEN) containing 1% 2-Mercaptoethanol and stored at -80°C for RNA extraction.

RNA sequencing and differential expression analysis

RNA was extracted using the QIAGEN RNeasy Micro Kit according to manufacturer's instructions. Library preparation and RNA-seq experiments were performed by the Genomic Unit of the Centre for Genomic Regulation (CRG, Barcelona, Spain). Depending on the cell type and stage, approximately 7,000-30,000 cells were required to obtain 1-2 ng of total RNA, which served as input for the library preparation using the SMARTer Ultra Low RNA Kit for ultra-low amount of RNA. The Illumina HiSeq 2000 platform was used to sequence libraries to a mean of approximately 50 million mapped 50 base pair single-end reads per sample. In the RNA-seq experiments, three biological replicates were ascertained for each dataset, except for oligodendrocytes where two replicates were used.

Bioinformatic analysis of RNA-seq data was performed by the Bioinformatic Unit at the CRG. RNA-seq quality check was performed using the tool FastQC (*41*). The goal of this step was to provide an overview of the quality of the data such as: per base sequence quality, GC content, duplication level, amount of overrepresented regions and presence of adapters. To confirm a low amount of rRNA contaminations, we extracted a subset of 1 million reads for every sample and aligned them against a database of rRNAs using the tool ribopicker (*42*). Consistent with the presence of a step for filtering by polyA selection in the RNA-seq protocol, we obtained a low amount of reads mapping to rRNAs (0.6-4.1%). Next, reads were aligned to the reference mouse genome (Ensembl release 66 corresponding to the Build 37 assembly, NCBIM37/mm9) using Tophat2 (*43*), a splice aware mapper for RNA-seq reads that uses known information of splicing events to align reads spamming the junction of two exons. We successfully mapped $75.2 \pm 13.5\%$ of the fragments to the genome.

Gene expression levels were reported in fragments per kilobase of transcript per million fragments mapped (FPKM) as a measure of the normalized abundances of transcripts. The Cufflinks method was used to compute FPKM values (*44*). FPKMs and read counts were scaled via the median of the geometric means of fragment counts across all libraries. Each replicated condition was used to build dispersion models, that were then averaged to provide a single global model for all conditions in the experiment. Differential expression analysis was performed using Cuffdiff2 to compare all pairs of conditions (*45*). The adjusted p-values for multiple comparisons (q-values or false discovery rate, FDR) were calculated using the Benjamini-Hochberg procedure as a method for multiple-testing correction. The cummeRbund R package from Bioconductor (*46*) was used for gene specificity analysis, data visualization, principal component (PC) analysis and Jensen-Shannon (JS) distance between replicates and samples. RNA-seq data have been submitted and have been assigned the following GEO accession number: GSE120161. R scripts for gene expression analyses are available on GitHub: https://github.com/rico-lab/synapdomain-favuzzi.

Analysis of gene expression specificity

To detect the genes that exhibit the highest degree of both subtype and stage specificity, we calculated specificity ratios for each cell population. We first selected all genes differentially expressed among P10 SST+ cells, P10 PV+ basket cells, and P10 chandelier cells, using a threshold of FDR < 0.05 for all pair comparisons with the other cell populations. To remove genes with high specificity owing to barely detectable expression, we additionally filtered them by a minimum normalized expression level (FPKM) of 10. Next, we further filtered our gene lists for each interneuron subtype by subsetting those genes that were developmentally upregulated between P5/8 and P10 stages. Finally, we ranked all significantly differentially expressed genes using a specificity ratio based on the fold change between the gene's normalized expression in a given interneuron subpopulation at P10 and the maximum expression level of that gene in the other cell types. The specificity ratio was calculated as the $\log_2$ transform of the fold change ($\log_2$FC) between the expression of a gene within a given interneuron population and the maximal expression across all other cell populations (*14*). For heatmaps in Figure 1E, we applied the specificity ratio to the three interneuron subtypes at both developmental stages (P5/8 and P10), interneurons at P0, pyramidal cells and oligodendrocytes. In these heatmaps, genes were ranked based on the gene specificity of the corresponding interneuron subpopulation at P10. For data visualization in the heatmaps in Figure 1B, we filtered genes by a minimum FPKM of 5, applied the specificity ratio to all populations at P10/12 and selected the top 100 genes.

A list of genes expressed in P12 pyramidal neurons but not in interneurons (*37*) was used as additional filter applied to the list of SST cell-specific genes. This was due to the labeling of a population of pyramidal cells in the lower layers of the more lateral somatosensory cortex of GIN mice (data not shown).

Of all genes exhibiting both subtype and stage specificity, we selected those that had a demonstrated or putative role in axon growth, axonal pathfinding, neuron-ECM communication or cell-cell adhesion, according to the gene ontology analysis or a manual MEDLINE® search.

Gene Ontology analysis

Gene Ontology (GO) analysis was performed to identify which gene classes distinguish SST+, PV+ basket and chandelier cells at P10. We used the "GOstats" and "ggplot2" R packages for data analysis and visualization, respectively. Differentially expressed genes between cell populations sorted at P10/P12 (interneuron subtypes, pyramidal cells, and oligodendrocytes) (FDR < 0.05) were used for the GO analysis. We applied a threshold of FPKM > 5 to remove genes with low expression levels. Specificity ratios were calculated for the three interneuron subpopulations at P10 as described above and genes exhibiting a $\log_2$ specificity ratio > 1.5 were selected. For the GO analysis relative to the Cellular Component category (Figure 1C and S3) the top 100 enriched genes for each interneuron subpopulation were used as input lists for the GO analysis. Enrichment scores for significant GO terms of the Cellular Component category were given as the $\log_{10}$ transformation of the p-value. For the GO analysis about the cellular functions (Figure 1D), the 50 most highly enriched genes were used as input.

Gene expression comparison with adult scRNAseq datasets

The "ggplot2" R package was used for violin plots depicting the gene expression of developmentally-regulated genes in single cell RNAseq studies from the adult cortex (*1*, *5*, *6*). To quantify the relative proportion of developmental genes that distinguish cell identities in the adult, we calculated the expression enrichment between the different clusters in each study. For Zeisel *et al*. 2015 (*5*), we divided the averaged expression of each candidate gene in single cells pooled from the SST+ clusters (named as "Int1", "Int2", and "Int4" in the original paper) and single cells pooled from the PV+ cluster (named as "Int3"). For Tasic *et al*. 2016 (*1*), we divided the averaged expression of each candidate gene in single cells pooled from the 6 SST+ cell types (yellow colours in the original paper) and single cells pooled from the 7 PV+ cell types (red colours in the original paper). For Paul *et al*. 2017 (*6*), we divided the averaged expression of each candidate gene in single cells pooled from a particular cell type (Martinotti cells, PV+ basket cells, or chandelier cells) and the mean expression between the other two cell types. Differential expression was set with a cut-off value of 2 for all three adult databases.

Interneuron-pyramidal cell molecular pairs

Cell-specific candidate molecules were selected based on their specificity ratio (calculated as described above) as well as synaptic role based on the gene ontology analysis or a manual MEDLINE® search. To obtain a longer input list, we eliminated some of the restrictions that were instead applied to obtain the top 5 molecules in Fig. 2A. In particular, we included molecules that were also expressed in P0 interneurons as well as molecules that did not show strong upregulation between P5/P8 and P10. To identify putative trans-synaptic partners, the list of cell-specific candidate synaptic genes was used as input in BioGRID (*47*) and STRING (*48*), two different databases of protein-protein interactions, as well as in a MEDLINE® search (see Table S4 for details). Among the interactors, only membrane proteins were selected (e.g. intracellular interactions were excluded). From the STRING database, only experimentally validated partners were selected. Interactors that appeared in STRING based on text mining were occasionally selected, i.e. only when the gene resulted expressed and highly enriched in pyramidal neurons. For each interactor, the expression level and specificity ratio in pyramidal neurons were computed. Only interactors that had FPKM > 5 in pyramidal neurons were reported. The specificity ratio was then used to rank the putative trans-synaptic partners and, consequently, the associated synaptic molecules.

Ternary diagrams

For each gene, a cell type specificity score was calculated based on the expression across the different interneuron subpopulations at both developmental stages (P5/8 and P10). Such specificity score is based on the JS divergence and quantifies the similarity between the expression profile of a given gene and the expression pattern of the extreme case in which a gene is present only in one population. We used this entropy-based metric as described before (*49*). The "cummeRbund" R package was used for calculating the specificity score that was then normalized to 1. The expression and specificity of protein family members were visualized in ternary diagrams by using the "ggtern" R package. In the relevant figures, the dot size corresponds to the maximum level of expression of each gene ($\log_2$FPKM+1) in the three subpopulations at P5/8 or P10. Differentially expressed

genes are represented with solid outlines (FDR < 0.05). Enriched genes are color-coded for a particular interneuron population based on the cell-type specificity score (>0.45). Gray colors identify genes that did not show enrichment for any interneuron subtype. Genes highlighted in bold show a 2-fold or higher upregulation in their expression levels (FPKM) between both developmental stages.

Quantitative real-time PCR

Total RNA was extracted from mouse brain tissue using TRIzol reagent (Invitrogen) followed by DNase I treatment (Promega). For *Cbln4* and *Lgi2* mRNA expression level analysis in Figure 2, *18S* was used as reference gene. For *Cbln4* and *Lgi2* mRNA expression level analysis on the infected mouse brain tissue in Fig. S12D, *mCherry* and *18S* were used as reference genes, respectively. We did not consider *mCherry* as the appropriate reference gene to assess *Lgi2* expression because, in contrast to *Cbln4*, not all infected mCherry+PV+ cells would also be Lgi2+. For *Lgi2* mRNA expression level analysis on the infected mouse brain tissue in Fig. S12D, to avoid contamination with Lgi2+ subplate neurons (that also express *Lgi2*) layer VI was excluded from the dissection when Lgi2 expression was assessed. cDNA synthesis was performed using the SuperScript IV First-Strand Synthesis System (Invitrogen) according to manufacturer's protocol. qPCR was carried out in triplicates on a LightCycler 480 Instrument (Roche) using SYBR Green PCR Master Mix (Roche). The sequences of qPCR primers were as follows: *Cbln4* (Fw: AGT CTA CCA GAG CCA AAC CAT CC, Rv: TTA GTG GCG GCT TCA CGG GTC AC), *Lgi2* (Fw: CAC CGT CTC TGA TGT GCT GTGT, Rv: ACT GGT ACG GCA GAG TCT GATG), 18S (Fw: GTA ACC CGT TGA ACC CCA TTC GT, Rv: GTG TGT ACA AAG GGC AGG GAC TTAA), *mCherry* (Fw: CAT CCT GTC CCC TCA GTT CATG, Rv: CAT CCT GTC CCC TCA GTT CATG), *Pcdh18* (Fw: CGG ACG GGA GAA TTC AGC CAG, Rv: TAG TCA GAG GAT GGC GAG GGC).

Perfusions and Immunohistochemistry

Animals were deeply anesthetized with sodium pentobarbital by intraperitoneal injection and then transcardially perfused with PBS followed by 4% paraformaldehyde (PFA) in PBS and prepared for free-floating immmunohistochemistry as described before (*25*). The following primary antibodies were used: rabbit anti-GAT-1 (1:250, Chemicon #AB1570), mouse anti-GAD67 (1:5000, Chemicon #MAB5406), mouse anti-AnkyrinG (1:500, NeuroMab #75-146), rat anti-somatostatin (1:200, Chemicon #MAB354), mouse anti-Reelin (1:250, MBL International #D223-3), rabbit anti-VIP (1:1000, ImmunoStar #20077), rabbit anti-nNOS (1:1000, ImmunoStar #24287), rabbit anti-calretinin (1:200, Chemicon #AB149), rabbit anti-GABA (1:2000, Sigma #A-2052), rabbit anti-Olig2 (1:250, Millipore #AB9610), mouse anti-GFAP (1:500, Sigma #G3893), goat anti-mCherry (1:500, Antibodies-Online #ABIN1440057), rabbit anti-NeuN (1:500, Millipore #ABN78), mouse anti-NeuN (1:500, Millipore # MAB377), goat anti-FGF13 (1:500, Santa Cruz #sc-16811), mouse anti-parvalbumin (1:1000, Sigma #P-3088), rabbit anti-parvalbumin (1:5000, Swant #PV-25), goat anti-parvalbumin (1:500, Swant #PVG-214); chicken anti-parvalbumin (1:500, SySy #195 006), rabbit anti-DsRed (1:500, Clontech #632496), chicken anti-GFP (1:1000, Aves Lab #1020), rabbit anti-VGAT (1:1000, SYSY #131 002), mouse anti-GAD65 (1:500, Millipore #MAB351R), rabbit anti-GluD1 (1:16000, kind gift from Ludovic Tricoire), mouse anti-Synaptotagmin-2 (1:250, ZFIN

#ZDB-ATB-081002-25), mouse anti-gephyrin (1:500, Synaptic Systems #147 011), guinea pig anti-ADAM22 (1:500, Synaptic Systems #317 005).

Fluorescent *In Situ* Hybridization Histochemistry

For dual-color fluorescent in situ hybridization combined with immunohistochemistry, mice were perfused and brains were fixed overnight in 4% PFA in PBS followed by cryoprotection in 30% sucrose-RNase free PBS and subsequent incubations as described before (*25*). The following DIG-labeled probes were used: *Cbln4* Fw: TAG AAC CCG ACT TCT CCG TGA TG and Rv: GCG ATA GAG TAT TCG ATT TCC CACC; *Lgi2* Fw: AGA TGA CAA ACT CCA CCG TCT and Rv: TAA AAC CCT TTG CTG TTC CAC; *Pcdh18* Fw: TCC ACC TCG CTT CCA GAG G and Rv: GGA TCT GCC ACC CG CAG. The following primary antibodies were used: chicken anti-GFP (1:500, Aves Lab #1020), rabbit anti-parvalbumin (1:5000, Swant #PV-25), rat anti-somatostatin (1:50, Chemicon #MAB354). *Dlx6a$^{Cre/+}$;Prox1-EGFP$^{+/F}$* (Jackson Laboratories #008199 and (*50*), respectively) as well as *VIP$^{Cre/+}$;RCE* (Jackson Laboratories #010908 and #32037, respectively) fate-mapped brains used for colocalizations with *Cbln4* and *Lgi2* mRNA were a gift from G. Fishell.

Cell Culture and Transfection

Cell lines. HEK293T cells were cultured in Dulbecco's Modified Eagle's medium supplemented with 10% fetal bovine serum, 2 mM glutamine, penicillin (50 units/ml) and streptomycin (50 g/ml). The cultures were incubated at 37°C in a humidified atmosphere containing 5% CO_2. HEK293T cells were transfected using polyethylenimine (PEI, Sigma) at a 1:4 DNA:PEI ratio.

Generation of AAV Expression Vectors

The *pDIO-DSE-mCherry-PSE-MCS* was engineered as follows: (1) the sequence containing the distal (DSE) and proximal elements (PSE) of the U6 promoter spaced by the CDS for mCherry was amplified by PCR (primers: Fw-TTC GCT AGC GGA TCC GGA ATA AC and Rv-CCA GAG GTT GAT GGT TTA TC AGGC); (2) the resulting PCR product was cloned into the *pAAV-EF1a-DIO-mCherry* vector (kindly provided by Prof. K. Deisseroth) and a TATA box was introduced in the U6 fragment (primers: Fw-TAT GCT TAC CGT AAC TTG AAA GTA TTT CGA TTT CTT GGG TTT ATA TAT CTT GTG GAA AGG ACG CGG TTT CCT AGG TTT AAA CTG and Rv- TAT GCT TAC CGT AAC TTG AAA GTA TTT CGA TTT CTT GGG TTT ATA TAT CTT GTG GAA AGG ACG CGG TTT CCT AGG TTT AAA CTG). The ssDNA primers to generate the *shRNAs* were obtained using the Block-it RNAi web tool (Thermo Scientific) and were as follows: *shGFP* (Fw: CTA GAA ATC GCT GAT TTG TGT AGT CCC TGA CCC AGA CTA CAC AAA TCA GCG ATT TTT TTG and Rv: AAT TCA AAA AGC CAC AAC GTC TAT ATC ATG GTG GGT CAG GCC ATG ATA TAG ACG TTG TGGC), *shLacZ* (Fw: cta gAA ATC GCT GAT TTG TGT AGT CCC TGA CCC AGA CTA CAC AAA TCA GCG ATT Ttt tttg and Rv: aat tca aaaa AAA TCG CTG ATT TGT GTA GTC TGG GTC AGG GAC TAC ACA AAT CAG CGA TTT), *shCbln4* (shRNA1 Fw: aat tca aaaa AAA TCG CTG ATT TGT GTA GTC TGG GTC AGG GAC TAC ACA AAT CAG CGA TTT and Rv: AAT TCA AAA AGC AAC AAG ACT CGC ATC ATT TTG GGT CAG GAA ATG ATG CGA GTC TTG TTGC;

shRNA2 Fw: CTA GGC TCC TGT ACC TGG ACA AAG ACC TGA CCC ATC TTT GTC CAG GTA CAG GAG CTT TTTG and Rv: AAT TCA AAA AGC TCC TGT ACC TGG ACA AAG ATG GGT CAG GTC TTT GTC CAG GTA CAG GAGC; shRNA4 Fw: CTA GGA CTC CAA GG GAT CAT CAT CTC CTG ACC CAA GAT GAT GAT CCC TTG GAG TCT TTT TG and Rv: AAT TCA AAA AGA CTC CAA GGG ATC ATC ATC TTG GGT CAG GAG ATG ATG ATC CCT TGG AGTC), *shLgi2* (shRNA1 Fw: CTA GGC AGC TGC TAT TGC TGA ATT CCC TGA CCC AGA ATT CAG CAA TAG CAG CTG CTT TTTG and Rv: AAT TCA AAA AGC AGC TGC TAT TGC TGA ATT CTG GGT CAG GGA ATT CAG CAA TAG CAG CTGC; shRNA2 Fw: CTA GGG AGA AGA AAC TCA ACG AAG TCC TGA CCC AAC TTC GTT GAG TTT CTT CTC CTT TTTG and Rv: AAT TCA AAA AGG AGA AGA AAC TCA ACG AAG TTG GGT CAG GAC TTC GTT GAG TTT CTT CTCC; shRNA3 Fw: CTA GGG GAC CAC ATA GAA ATG AAT TCC TGA CCC AAA TTC ATT TCT ATG TGG TCC CTT TTTG and Rv: AAT TCA AAA AGG GAC CAC ATA GAA ATG AAT TTG GGT CAG GAA TTC ATT TCT ATG TGG TCCC; shRNA4 Fw: CTA GGC TCT CAC ATT TAC AAA TAC GCC TGA CCC ACG TAT TTG TAA ATG TGA GAG CTT TTTG and Rv: AAT TCA AAA AGC TCT CAC ATT TAC AAA TAC GTG GGT CAG GCG TAT TTG TAA ATG TGA GAGC; shRNA5 Fw: CTA GGC AGA ACA CCC TCT ACC TTT CCC TGA CCC AGA AAG GTA GAG GGT GTT CTG CTT TTTG and Rv: AAT TCA AAA AGC AGA ACA CCC TCT ACC TTT CTG GGT CAG GGA AAG GTA GAG GGT GTT CTGC), *shFGF13* (shRNA2 Fw: CTA GGC ACT TAC ACT CTG TTT AAC CCC TGA CCC AGG TTA AAC AGA GTG TAA GTG CTT TTTG and Rv: AAT TCA AAA AGC ACT TAC ACT CTG TTT AAC CTG GGT CAG GGG TTA AAC AGA GTG TAA GTGC; shRNA4 Fw: CTA GGC AAT GAA CAG CGA GGG ATA CCC TGA CCC AGT ATC CCT CGC TGT TCA TTG CTT TTTG and Rv: AAT TCA AAA AGC AAT GAA CAG CGA GGG ATA CTG GGT CAG GGT ATC CCT CGC TGT TCA TTGC; shRNA6 Fw: CTA GGG CAA GAC CAG CTG CGA CAC CTG ACC CAT GTC GCA GCT GGT CTT GCC TTT TTG and Rv: AAT TCA AAA AGG CAA GAC CAG CTG CGA CAT GGG TCA GGT GTC GCA GCT GGT CTT GCC from (*21*)), *shPcdh18* (shRNA1 Fw: CTA GGC ACT TTA GAT TTG CAC TTG CCC TCA CCC AGC AAG TGC AAA TCT AAA GTG CTT TTT G and Rv: AAT TCA AAA AGC ACT TTA GAT TTG CAC TTG CTG GGT GAG GGC AAG TGC AAA TCT AAA GTG C; shRNA2 Fw: CTA GGC AGC TTC TTA CAA TAC ACC TCA CCC ATG TAT TGT GTA AGA AGG CTG CTT TTT and Rv: AAT TCA AAA AGC AGC TTC TTA CAA TAC ATG GGT GAG GTG TAT TGT GTA AGA AGG CTG CG; shRNA3 Fw: CTA GGC TGT GTT GCT GGT TAT TAT GCC TCA CCC ACA TAA TAA CCA GCA ACA CAG CTT TTT G and Rv: AAT TCA AAA AGC TGT GTT GCT GGT TAT TAT GTG GGT GAG GCA TAA TAA CCA GCA ACA CAG C; shRNA4 Fw: CTA GGG GAG AAT TCC AGC AGC AAT GCC TCA CCC ACA TTG CTG CTG GAA TTC TCC CTT TTT G and Rv: AAT TCA AAA AGG GAG AAT TCC AGC AGC AAT GTG GGT GAG GCA TTG CTG CTG GAA TTC TCC C; shRNA5 Fw: CTA GGC ATT CTC ATC AGG GCC TTG ACC TCA CCC ATC AAG GCC CTG ATG AGA ATG CTT TTT G and Rv: AAT TCA AAA AGC ATT CTC ATC AGG GCC TTG ATG GGT GAG GTC AAG GCC CTG ATG AGA ATG C). To minimize the putative off-target effects of the shRNA, a miR-133 derived loop sequence was used (*51*). The shRNAs targeting FGF13 (shRNA-2 and

shRNA4) were obtained from previous studies (*21*). Both shRNAs are designed to downregulate the expression of the two known isoforms of FGF13, *Fgf13A* and *Fgf13B*. For the rescue experiments, a triple vector containing the shRNAs, mCherry and the *shRNA*-resistant full-length proteins were generated. The coding sequences for *Cbln4*, *Lgi2* and *Fgf13* full-length were obtained from P30 mouse hippocampal cDNA and cloned into the pGEMT-easy vector (Promega). *Fgf13A* and *Fgf13B* isoforms were subcloned for the subsequent rescue experiments. The shRNA resistant proteins were designed and ordered via GeneArts (ThermoFisher) in order to have 5 synonymous mutations to each shRNA and a HA tag sequence. These DNA sequences were cloned in the *pDIO-DSE-mCherry-PSE-MCS* after adding a T2A sequence generating the *pDIO-DSE-mCherry-T2A-mutFull-length-PSE-MCS (shRNA)* plasmid (Fig. S12).

<u>AAV Production and In Utero/Intracranial Injections</u>

AAV Production. HEK 293FT cells (ThermoScientific) were seeded on 15-cm plates and co-transfected with packaging plasmids AAV-ITR-2 genomic vectors (7.5µg), AAV-Cap8 vector pDP8 (30 µg; PlasmidFactory GmbH, Germany, #pF478) or AAV-Cap DJ Rep-Cap vector (30 µg; Cell Biolabs, VPK-420-DJ) using PEI (Sigma) at a ratio 1:4 (DNA:PEI). 72 hours post transfection, supernatants were incubated with Ammonium sulfate (65g/200ml supernatant) for 30 minutes on ice and centrifuged for 45 minutes at 4000 RPM at 4°C. Transfected cells were harvested and lysed (150mM NaCl, 50mM Tris pH8.5), followed by three freeze-thaw cycles and Benzonase treatment (50U/ml; Sigma) for 1 hour at 37°C. Filtered AAVs (0.8 µm and 0.45 µm MCE filters) from supernatants and lysates were run on an Iodixanol gradient by ultracentrifugation (Vti50 rotor, Beckmann Coultier) at 50,000 RPM for 1 hour at 12°C. The 40% iodixanol fraction containing the AAVs was collected, concentrated using 100 kDa-MWCO Centricon plus-20 and Centricon plus-2 (Merck-Millipore), aliquoted and stored at -80°C. The number of genomic copies was determined by qPCR using the following primers against the WPRE sequence: Fw: GGC ACT GAC AAT TCC GTG GT and Rv: CGC TGG ATT GAG GGC CGAA). AAVs with a titer equal or higher to 10^{11} genome copy/ml were used for in vivo injections. For down-regulation experiments, two shRNAs producing a good *in vitro* downregulation were used for each gene. The two shRNA plasmids were co-transfected for AAV production in order to increase the downregulation efficiency. The *AAV8-hSyn-FLEX-Chronos-GFP* and *AAV9-hSyn-eGFP* were acquired from the Penn Vector Core, with a titer of 4.60 x 10^{12} genome copy/ml and 8.88 x 10^{12}, respectively.

Intracranial injections. For intracranial injections, P2 (*Nkx2-1^{CreER/+}* and *PV^{Cre/+}*) or P3 (*Lhx6^{Cre/+}* and *Sst^{Cre/+}*) pups were anesthetized with isoflurane and mounted on a stereotactic frame using a 3D printed isoflurane mask. Unilateral or bilateral stereotaxic injections of the Cre-dependent viruses at rate of 100 nl/minute followed by 2 additional minutes to allow diffusion were carried out as follows. For SST interneuron experiments: *AAV8-shCbln4-mCherry*, *AAV8-shCbln4-mCherry-T2A-mCbln4-HA* or *AAV8-shLacZ-mCherry* or dual injections with *AAV8-shCbln4-mCherry* and *AAV8-Chronos-GFP* were injected in the somatosensory cortex (anteroposterior –2.5/ -2.7 mm; mediolateral +2.1/2.3 mm; dorsoventral –0.5 and –0.2 mm relative to Bregma) of *Sst^{Cre/+}* mice. For PV basket cell experiments: *AAV8-shLgi2-mCherry*, *AAV8-shLgi2-mCherry-T2A-mLgi2-HA* or *AAV8-shLacZ-mCherry* were injected in the somatosensory cortex (anteroposterior –2.5/ -2.7 mm; mediolateral +2.1/ 2.3 mm; dorsoventral –0.5 relative to Bregma) of

Lhx6$^{Cre/+}$ mice. For chandelier cells experiments: *AAV8-shFgf13-mCherry*, *AAV8-shFgf13-mCherry-T2A-mFgf13A-Flag*, *AAV8-shFgf13-mCherry-T2A-mFgf13B-HA* or *AAV8-shLacZ-mCherry* were injected in the medial prefrontal cortex (anteroposterior −0.6 mm; mediolateral +0.2 mm; dorsoventral −0.4 and −0.8 mm relative to Bregma) in *Nkx2-1$^{CreER/+}$* or *PV$^{Cre/+}$*. All viruses used for injection were serotype 8 with the exception of the experiments performed with *Sst$^{Cre/+}$* where data from mice injected with AAV8 or AAV-DJ 2 were pooled because no difference was found between them.

Over- and ectopic- Cbln4 expression experiments were performed injecting a Cre-dependent virus expressing *Cbln4-HA* in *Sst$^{Cre/+}$*, *PV$^{Cre/+}$* and *Nkx2-1$^{CreER/+}$* mice. Dual injections of *AAV9-hSyn-eGFP* together with *AAV8-DIO-mCbln4-HA* allowed the labeling of the pyramidal cells for the quantification of PV somatic and chandelier inputs.

In utero injections. In utero injections for morphological reconstructions were performed as described previously (*37*). Briefly, we obtained isolated cells by injecting 1 µL of AAVs diluted 1:30 in PBS with FastGreen 0.5%, into the telencephalic lateral ventricle of E14.5 *Sst$^{Cre/+}$* or E15.5 *Lhx6$^{Cre/+}$* embryos. Pregnant females were deeply anesthetized with isoflurane (5% induction, 2% maintenance), the abdominal cavity was cut opened and the uterus exposed making the embryos accessible. After injection, the uterus was placed back in the abdominal cavity, the incision was sutured and buprenorphine 0.1 mg/kg was used for analgesia.

Western blot and co-immunoprecipitation

For western blot analysis, HEK293T were rinsed with 1x ice-cold PBS. Samples were homogenized in lysis buffer containing 25 mM Tris-HCl pH 8, 50mM NaCl, 1% Triton X-100, 0.5% sodium deoxycholate, 0.001 % SDS and protease inhibitor cocktail (cOmplete Mini, Roche). Samples were resolved by SDS-PAGE and transferred onto PVDF membranes. Membranes were blocked with 5% Blotting-Grade Blocker (Bio-Rad, #1706404) in TBST (20mM Tris-HCl pH7.5, 150mM NaCl and 0.1% Tween20) for 1 hour and probed with the following primary antibodies overnight at 4°C: rabbit anti-actin (1:1000, Sigma #A2066), mouse anti-HA (1:500, Thermo Fisher #26183), rabbit anti-GluD1 (1:5000, kind gift from Ludovic Tricoire), guinea pig anti-ADAM22 (1:1000, Synaptic Systems #317 005). After incubation with HRP-conjugated secondary antibodies, protein levels were visualized by chemiluminescence. Blots were scanned using a LI-COR Odyssey® Fc Imaging System or a ChemiDoc (Bio-Rad).

For co-immunoprecipitation (co-IP) experiments, 900,000 HEK cells were transfected with 4 µg of Cre expressing plasmid and 4 µg of Cre-dependent plasmid expressing *Cbln4*-HA, *Lgi2*-HA or mCherry (8 µg of total DNA) using Lipofectamine 2000 Transfection Reagent (Thermo Fisher, 12566014) according to manufacturer's instructions. Supernatants and lysates were collected 4 days after transfection and mixed with 600 µg of cortical homogenates from P30 mice. The mix was then diluted in 1 ml of Co-IP buffer (0.3M sucrose, 10 mM Tris-HCl pH 8, 10 mM NaCl, 3 mM MgCl2, 1% NP-40, 5% glycerol and protease inhibitor cocktail) and subsequently incubated with 30 µl of anti-HA magnetic beads (Thermo Fisher, 88836) at 4°C for 2 hours (preclearing). The precleared mix was then subsequently incubated overnight at 4°C with 30 µl of anti-HA magnetic beads (Thermo Fisher, 88836). After overnight incubation at 4°C with gentle rotation, the beads were rinsed six times with Co-IP buffer. Immune complexes were then analyzed by western blot. Since in most experiments both Adam22 and GluD1

appeared to bind the HA-beads despite preclearing and a high number of washes, the co-IP success was defined as such when the fold change between the amount of immunoprecipitated partner in the IP containing the protein of interest (Lgi2 or Cbln4) was at least 1.5 folds higher than that found in the IP without the protein of interest.

<u>Image acquisition and analysis</u>

For imaging analysis, tissue samples were imaged on an inverted Leica TCS-SP8 confocal maintaining same laser power, photomultiplier gain, pinhole, and detection filter settings (1024x1024 resolution, 8 bits or 16 bits for fluorescence intensity quantifications). Cell co-localization analyses were carried out using confocal image stacks (40X oil immersion objective, 1.4 NA, 0.2 μm step size) and analyzed using a custom macro in Fiji (ImageJ) software. Counting of the number of interneurons per layer and the cell co-localization analyses based on in situ hybridizations were performed manually. Fluorescence intensity analysis in Figure 2 was performed in the prefrontal cortex as described before (*25*). For synaptic analysis, confocal image stacks were taken (100X oil immersion objective, 1.44 NA, 2.2 digital zoom, 0.2 μm step size) and analyzed at P28-P30 with IMARIS 7.5.2 software for all experiments, except for Fig. S1, S13 and S19 where Image J was used as described before (*25*).

For the analysis of synaptic inputs made by the SST cells, we analyzed synapses in layer I, which contains the apical tufts of mainly layer V but also (less abundant) layer II/III pyramidal neurons (*52*). For PV+ basket cells synapses, because *Lgi2* is more expressed in lower layers, we focused our analysis on nearby pyramidal cells located in layer V. For chandelier synapse analysis, because we mainly label chandelier cells located in layer II, we analyzed axo-axonic synapses onto nearby pyramidal cells, i.e. located in layer II/III.

For all analyses performed in Imaris, threshold values were calculated and applied in the same way for all brains or cells within each experiment (i.e. for all brains/cells belonging to both control and knockdown/overexpression). Unless otherwise stated, threshold values were calculated individually for each brain using the "above automatic threshold" tool in Imaris. For the majority of experiments, an average threshold among these individual values was computed and applied to all images. When >2 individual threshold values were more than 5 "Quality" units apart, the individual threshold values were used. Such values were automatically established ("above automatic threshold" tool) in Imaris in the non-injected hemisphere or in the injected hemisphere for brains that had bilateral injections.

For the analysis of synaptic inputs made by the SST cells, we quantified the density of synapses within the Somatostatin axon labeled with mCherry. These axons were reconstructed with the "create surface" tool. Briefly, mCherry+ axons included within the tissue sections were isolated in three dimensions. Three-dimensional isosurfaces were created using the "create surface" tool and volume was quantified automatically. An automatic threshold was selected to include as much of the axon as possible while excluding any background and a 0.02 μm^3 size filter was applied. Then, we used GAD65+ as a presynaptic marker, and applied the "spot" tool to detect the GAD65+ boutons within the surface using a threshold automatically established in Imaris ("above automatic threshold" tool) and a spot diameter of 0.6 μm. These boutons were quantified

as synapses when they were colocalizing with Gephyrin+ boutons (spots above automatic threshold, diameter of 0.3 μm).

For the analysis of the PV cell outputs, we analyzed the Syt2+ somatic boutons within mCherry+ terminals contacting the NeuN+ soma of putative pyramidal cells. mCherry+ axons were automatically reconstructed using the "create surface" tool and NeuN+ somata were manually reconstructed using the "draw surface" tool. Syt2+ spots (spot diameter of 0.8 μm) within the surface of mCherry+ axons were considered PV synaptic terminals. Then, we used the tool "spots close to surface" (ImarisXT extension) to filter the spots located at 0.4 μm from the NeuN surface. Somatic Syt2+ boutons from infected cells were identified using "Split spots into surface" tool. Since the number of double-positive mCherry+Syt2+ boutons depends on the infection efficiency, we normalized bouton density to the number of infected PV+ cells in the area.

For the analysis of chandelier cells, the axon initial segment (AIS, labeled with AnkyrinG) was reconstructed with the "create surface" tool as described above. A size filter was applied with the minimum size being related to the volume of the AIS. For bouton density, the chandelier presynaptic boutons were detected with the "spot" tool using a spot diameter of 0.7 μm and a threshold was manually selected to accurately detect as many spots as possible without creating artifacts (i.e. only the synaptic varicosities within a cartridge would be detected). The radius of the spot was used as a threshold distance to define the contact with the AIS and the "Find spots close to surface" tool (ImarisXT extension) was used to count the number of presynaptic boutons ("spots") that were contacting the surface of the AIS.

A cartridge was defined as such when at least 3 consecutive presynaptic boutons were found on the same chandelier axonal segment. For each cartridge, we measured length, number of boutons per cartridge, number of AISs contacted by one cartridge and the 'distance to closest cartridge' parameter. Cartridge length was quantified by tracing a line that joined all consecutive varicosities found on each cartridge and automatically measuring its length. The number of boutons in each cartridge was determined by counting the number of varicosities found in the entire length of each cartridge. The number of AISs contacted by one cartridge was assessed by calculating the total number of AISs contacted by one cartridge (with 'cartridge' and 'contact' defined as above) within the field of view. The 'distance to closest cartridge' indicates the average distance between each cartridge and the cartridge that is closest to it. This parameter is considered diagnostic of the overall density of the cartridges in a given volume and was used as a proxy to estimate the density of the chandelier arbor (53).

Note that we used two different Cre drivers to downregulate *Fgf13* in chandelier cells. First, *Fgf13* was downregulated early using *Nkx2-1CreER/+*. Since *Fgf13* downregulation resulted in both axonal disorganization and synaptic loss, we could not rule out that the observed synaptic phenotype was merely a consequence of the disorganized chandelier axonal arborization rather than a deficit in synapse formation (e.g. since each AIS is innervated by more than one cartridge (54) and the axonal arbor is less dense upon *Fgf13* downregulation, the resulting average synapse density onto the AIS may be correspondingly scaled down). Then, we took advantage of the *PVCre/+* line, which turned on the expression of Cre at later stages of development (after P14) and therefore downregulated *Fgf13* when the axon was almost fully developed. This approach

has also been used by others in the past to tell apart axonal and synaptic phenotypes in chandelier cells (*55*).

The analysis of dendritic synapses made by PV+ basket or chandelier cells was performed as detailed above with the exception that the target dendrites (labeled by *AAV9-hSyn-eGFP* viral injection) were reconstructed with the "create surface" tool.

The analysis of SST+ synapses onto the proximal and distal dendrites shown in Figure S13 was performed as follows: single focal planes containing consecutive dendritic segments of a total length ≤ 10 μm were analyzed using a custom Image J macro similarly to what described before (*25*). Briefly, processing of all channels included background, subtraction, gaussian blurring, smoothing and contrast enhancement. All single channel images were converted to RGB. For the pyramidal cell dendrite, a color threshold was selected to identify the dendritic surface. The border of the dendrite was manually drawn to automatically calculate its area and create a mask with the dendrite only. For the mCherry+ or GAD65+ presynaptic boutons, a color threshold was selected to include as many putative synapses as possible while excluding any background. The "Analyze Particles" (size 0.20-infinity, circularity 0.00-1.00) tool was applied and a mask was generated. A merged image from all masks was created. Presynaptic boutons (mCherry+GAD65+) were defined as such when at least 50% of the signal from the two channels was overlapping. Contacts (mCherry+ terminals or mCherry+GAD65+ boutons) were defined as such when they were located outside the perimeter border but had ≥ 1 pixel colocalizing with the mask of the dendrite. For dendritic segments shorter than 10 μm, data from consecutive focal planes were analyzed until a total 10 μm length was reached. Data were collected as density (number of mCherry+GAD65+ presynaptic boutons or mCherry contacts per unit of dendritic surface) and the density data from each segment were used to generated cumulative plots (Fig. S13B and E). Data from segments within 40 μm from the soma were used to compute the average density for the proximal dendrites whereas data from segments located further than 40 μm were pooled to compute the average density onto the distal dendrites (Fig. S13 C and F). For the linear regression analysis in Fig S13D and G, the average density in each segment (segment length 10 μm, total length 100 μm) was computed for each cell and the results were used to perform the linear regression analysis.

For the analysis of PV+ basket synapses using *Nkx2-1$^{CreER/+}$* in Figure S17A (right bar graph), mCherry+PV+ cells were identified and their axons were followed and imaged. Imaris reconstruction was performed as described above and, to exclude axons belonging to other cells, only axons making at least one Sty2+Gephyrin+ synapse were used to compute the volume of the presynaptic axon.

For the synaptic colocalization graphs in Figure S19, a similar custom Image J macro was used with the exception that the output was the fraction of colocalizing particles. The synaptic profile plots in Figure S19 were generated using ImageJ as follows: a line (perpendicular to the synaptic cleft) was drawn starting just before the presynaptic site (x=0, to be able to obtain the background level) until slightly after the end of the postsynaptic cluster and the command "plot profile" (under "Analyze") was used in "live mode" in such a way that the grey values for each channel were automatically computed along the line. The analysis performed in Figure S19 was

focused on *Cbln4* and *Lgi2* because these were the proteins for which a putative trans-synaptic partner had been shown.

<u>Reconstruction and analysis of morphology</u>

Infected mCherry+ isolated neurons were stained and imaged on an Apotome.2 (Zeiss) maintaining the same settings (1024x1024 resolution, 8 bits) and using a 20X objective (1.4 NA, 0.8 μm step size). The morphological evaluation was focused on Martinotti and PV+ basket cells located in layer V, since the synaptic analysis was mostly performed on the output of layer V interneurons (see Image acquisition and analysis section for synaptic analysis). The neuron's processes were traced automatically and quantified using a modification of a custom Matlab script described before (*56*).

<u>*In vitro* Patch-Clamp Recordings</u>

Slice Preparation. Mice (P28-P50) were transcardially perfused with ice-cold NMDG (*57*) cutting solution (in mM: 93 NMDG, KCl 2.5, NaH_2PO_4 1.2, $NaHCO_3$ 30, HEPES 20, Glucose 25, Sodium Ascorbate 5, Thiourea 2, Sodium Pyruvate 3, $MgSO_4$ 10, $CaCl_2$ 0.5). The brain was quickly removed and slices cut under the same solution as used for perfusion. Parasagittal slices were cut by making an incision on the right (non-injected) hemisphere, angled 10-15 degrees with the midline (towards lateral side, away from experimenter). The brain was glued to the stage on this cut surface and 300 μm slices were cut using a vibratome (Leica). Slices were transferred to a heated chamber (34 C°) containing cutting solution, where they underwent recovery for either 5 (current-clamp recordings) or 12 minutes (voltage-clamp recordings). Slices were then moved to an incubation chamber containing room-temperature, oxygenated holding solution (NaCl 92, KCl 2.5, NaH_2PO_4 1.2, $NaHCO_3$ 30, HEPES 20, Glucose 25, Sodium Ascorbate 5, Thiourea 2, Sodium Pyruvate 3, $MgSO_4$ 2, $CaCl_2$ 2), where they remained for an additional 40 minutes, and throughout the day, before being individually transferred to the recording chamber for experiments.

Experimental conditions. All recordings were carried out at 32-34 C°. Before recording, slices were quickly screened for infection with the virus, and slices peripheral to the main area of infection were discarded. In most cases, 3 slices with strong and consistent infections were kept per animal. Care was taken to record from regions with dense infection, as visualized with infrared-differential interference optics (Hamamatsu camera controller) and fluorescence illumination (Cool Led 473nm) through a 10x or 40x water-immersion objective (Olympus). All neurons were recorded in S1 barrel field layer 5 in artificial cerebrospinal fluid (NaCl 127, KCl 2.5, $MgSO_4$ 1.298, NaH_2PO_4 0.625, $NaHCO_3$ 26, Glucose 13, $CaCl_2$ 2).

Pipettes were pulled from borosilicate glass (1.5 mm outer diameter x 0.86 mm inner diameter; Harvard Apparatus) on a vertical Narishige PC10 puller to obtain a tip resistance of 4-6 MΩ. For voltage-clamp recordings from pyramidal cells, Cesium Methanesulfonate solution was used (Cesium Methanesulfonate 135, KCl 8, HEPES 10, Mg-ATP 0.4, Na_2-ATP 2.0, EGTA 0.5, Na-GTP 0.64, Qx-314 Chloride 5), whereas for current-clamp recordings from SST+ interneurons Potassium Gluconate solution was employed (Potassium Gluconate 130, KCl 5, HEPES 10, $MgCl_2$ 2, di-sodium phosphocreatinine 10, Na_2-ATP 2, Na-GTP 0.64). For any experiment, only cells with access resistance < 20MΩ were accepted. The experimental protocol deployed per cell

lasted 10-20 minutes. Access resistance was monitored throughout using seal tests and any cells where access resistance deteriorated and increased above 30 MΩ were discarded. For pyramidal recordings, after breakthrough, a period of 3-5 minutes was allowed, for dialysis of the solution into the neuron. During this period, access resistance was monitored and improved if required. Prior to recording, voltage-clamped cells were held at -65 mV and slowly depolarised to an experimental holding potential of +40 mV, chosen to increase the driving force for chloride in order to enable easier detection of GABAergic input onto dendrites of pyramidal neurons. Data were filtered on-line at 2 kHz, and acquired at a 50 kHz sampling rate using a MultiClamp 700B amplifier and Digidata 1440 digitiser (Axon Instruments).

Optogenetics. All experiments were conducted under wide-field photostimulation (*58*) through a 40x water-immersion objective. Measurements of irradiance were taken regularly prior to beginning experiments with a power meter mounted underneath the recording chamber's fluid-filled coverslip (without a slice). The recorded neuron was centred in the field of view. A 473nm LED was triggered to deliver a square-shaped pulse of 1 ms illumination at irradiance values of: 21.2, 17.7, 13.6, 9.3, 4.4, 2.0, 0.9 and 0.2 mW/mm2. For every cell and irradiance value, we recorded 10 trials of photostimulation, which was delivered every 2 seconds. Glutamate receptors were blocked with 40μM D-APV and 40μM CNQX. For minimal stimulation experiments[2], irradiance was systematically lowered in small steps (0.02-0.05 mW/mm2) until stimuli no longer elicited IPSCs in the expected response window. At this point, irradiance was increased stepwise until a mixture of failures and events of reliable amplitude and latency was observed. Once minimal irradiance was established, 50 trials of minimal stimulation were acquired per cell. There were no statistically significant differences in failure rate between the Control (66.7 ± 3.5%) and Knockdown (71.0 ± 2.4%) groups ($p = 0.3224$, t = 1.0, df = 34, Student's t-test), indicating pre-synaptic SST neurons were similarly engaged by photostimulation.

Data Analysis. The time window of optogenetically-evoked spiking was determined from recordings of SST+ interneurons expressing ChR2 in Control and Knockdown groups. At the highest irradiance used, latency to spike peak (relative to photostimulus onset) was 1.99 ± 0.54 ms and 2.28 ± 0.38 ms for respectively Control and Knockdown groups (no statistically significant difference; $p = 0.1932$, Mann-Whitney U = 106). For the lowest intensity that reliably elicited spikes (0.9 mW/mm2), these values were 4.05 ± 0.62 ms and 4.70 ± 0.59 ms (no statistically significant difference; $p = 0.2939$, Mann-Whitney U = 86). To ensure we captured IPSCs potentially occurring in distal dendrites, our even detection window encompassed the period of 2-20 ms after photostimulus onset. Within this window, we manually detected, extracted and analysed the earliest-occurring IPSC using Minianalysis (Synaptosoft). Optogenetically-evoked IPSCs were clearly time-locked and showed little trial-to-trial variability, making their detection and separation from spontaneous events straightforward, when aligning recording traces to photostimulus onset (see Fig. 4 for example traces). IPSC peak amplitude, peak time and 10-90 rise time were averaged across the 10 sweeps at each irradiance per cell. IPSC onset time was approximated by subtracting 10-90 rise time from peak time. Average values per cell were then condensed into a grand average per group.

For minimal stimulation experiments, the same procedure was applied to obtain event detection windows. Latency to spike was 11.1 ± 0.64 ms and 12.4 ± 0.74 ms for

Control and Knockdown groups respectively (no statistically significant difference; $p = 0.396$, Mann-Whitney U = 121). We therefore used an IPSC detection window of 10-30 ms after stimulus onset. IPSCs were detected manually as outlined above. Since minimal stimulation IPSCs are lower amplitude and occur under a regime of mixed successes and failures, distinction from spontaneously-occurring events is challenging. Therefore, for minimal stimulation experiments we extracted and analysed any IPSC event occurring within the detection window. Keeping this window narrow helped us lower the probability that spontaneous events "contaminated" our analysis.

Intrinsic properties of SST+ interneurons were measured rapidly after obtaining whole-cell configuration. A series of depolarizing or hyperpolarizing 500 milliseconds current steps were used at 0.5 Hz. Resting membrane potentials were measured just after patched membranes were ruptured by suction. Input resistance and membrane time constants were determined by passing hyperpolarizing current pulses inducing voltage shifts of 5-15 mV negative to resting membrane potential. Time constants were measured by fitting voltage responses with a single exponential function. Action potential (AP) threshold was determined as the voltage at which the first derivative of voltage over time exceeded 20 mV/ms. AP widths at half amplitude were measured for spikes elicited by depolarizing current pulses of threshold strength. Rheobase was determined by initially injecting positive current generating near-threshold 15-25 mV depolarizations and subsequently applying 1 pA current steps until APs were elicited. Rheobase was considered to have been reached once three such steps consecutively produced an AP, with the lowest value of the AP-generating injected currents used. Delay to first AP was measured during the same procedure, as the time elapsed between onset of current injection and AP threshold and was calculated from the average of 4 repetitions of this procedure. AP height was calculated as the difference in membrane potential between AP threshold and the peak. Afterhyperpolarisation (AhP) amplitude was defined as the difference between AP threshold and the most negative potential attained within 5 milliseconds of AP threshold. AhP time was defined as the time elapsed between this point and AP threshold. Maximum firing frequency and input-output curves were obtained by injecting steps of 50-100 pA current. AP frequency adaptation was calculated as the percent change in spike frequency during the last 100 milliseconds of the spike train compared to the first 100 milliseconds.

Statistical analysis

All statistical analyses were performed using GraphPad Prism 6 (GraphPad Softwares) or SPSS (IBM Corp) softwares. Normality was assessed using the Shapiro-Wilk normality test. Unless otherwise stated, parametric data were analyzed by *t*-test or one-way ANOVA followed by Holm-Sidak or Tukey *post hoc* analysis for comparisons of multiple samples. Non-parametric data were analyzed by the Mann-Whitney rank sum test or Kruskal-Wallis one-way analysis of variance on ranks followed by Holm-Sidak or Dunn *post hoc* analysis for comparisons of multiple samples. Probability distributions were compared using the Kolmogorov-Smirnov test. P values <0.05 were considered statistically significant. Data are presented as mean ± SEM.
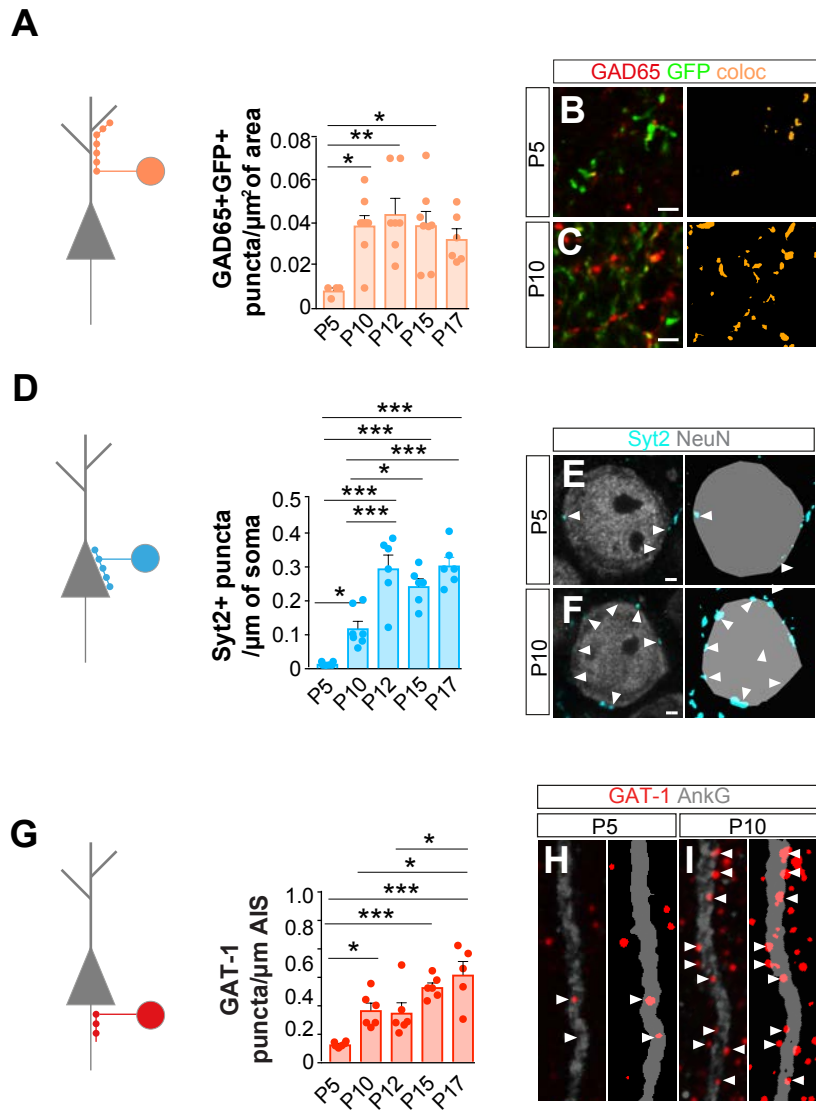
Figure S1

Fig. S1. Development of different types of inhibitory synapses over time.
(**A** to **C**) Schematic, density, representative image and corresponding thresholded mask used for quantification of GFP+ GAD65+ presynaptic boutons per unit of area at different stages of early postnatal development in layer I of the mouse somatosensory cortex where the majority of dendritic inhibitory synapses are made by Martinotti cells on the terminal tuft dendrites of pyramidal cells (n ≥ 4 *SST-Cre::RCE* mice for each stage). (**D** to **F**) Schematic, density, representative image and corresponding thresholded mask used for quantification of Syt2+ presynaptic boutons around the soma of NeuN+ pyramidal neurons in layer II/III of the mouse somatosensory cortex at different stages of early postnatal development (n ≥ 6 mice for each stage). (**G** to **I**) Schematic, density, representative image and corresponding thresholded mask used for quantification of GAT1+ presynaptic boutons contacting the postsynaptic axonal initial segment (AIS) scaffold protein Ankyrin G (AnkG) at different stages of early postnatal development in layer II/III of the mouse prefrontal cortex (n ≥ 5 mice for each stage). *p<0.05, **p<0.01, ***p<0.001, One-way ANOVA followed by Tukey's multiple comparisons test.. Scale bar equal 2 μm (**B**, **C**, **E**, **F**) and 1 μm (**H** and **I**).
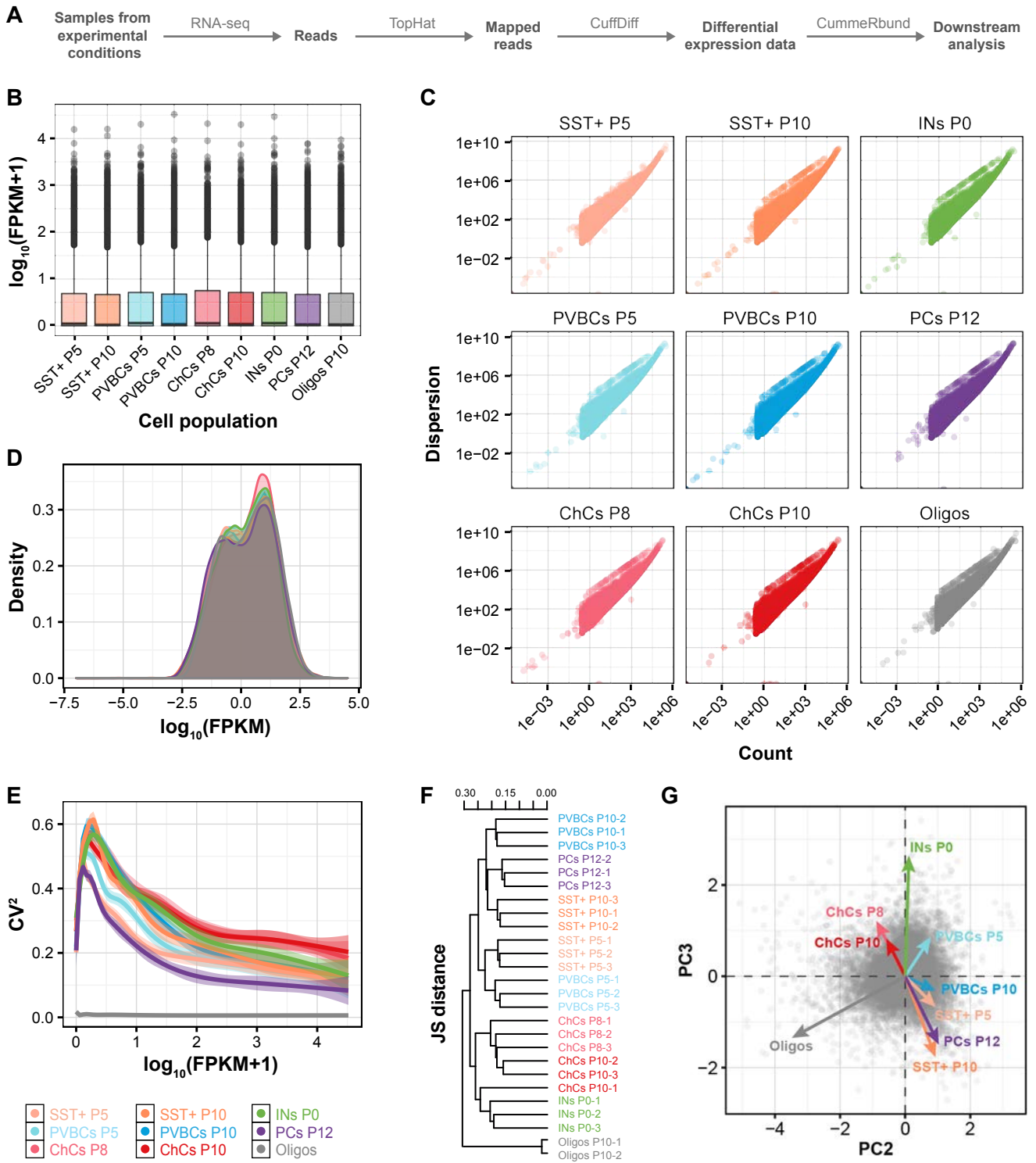
Figure S2

Fig. S2. Validation of RNA-seq experiments.

(**A**) Diagram illustrating the RNA-seq analysis workflow. (**B**) Bar graph showing a similar dispersion of total mRNA expression in the different cell populations. (**C**) Similar dispersion patterns of counts in the different cell populations and stages. (**D**) The distributions of FPKM scores are comparable across samples. (**E**) The squared coefficient of variation shows low cross-replicate variability between cell populations and stages. (**F**) Unsupervised hierarchical clustering based on the Jensen-Shannon (JS) distance of the complete RNA-seq transcriptome data reveals low distance among replicates and higher distance across cell types. (**G**) Principal component (PC) analysis on individual gene levels (FPKM) indicates that cell-type and developmental stage were the greater sources of variability in gene expression.
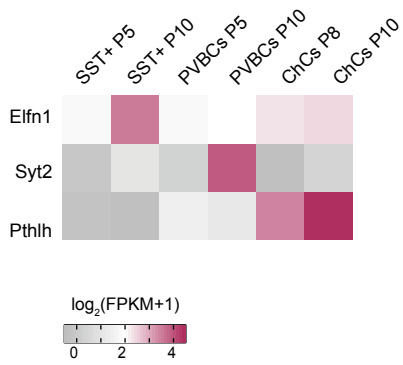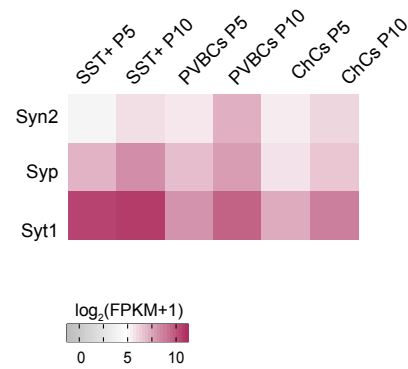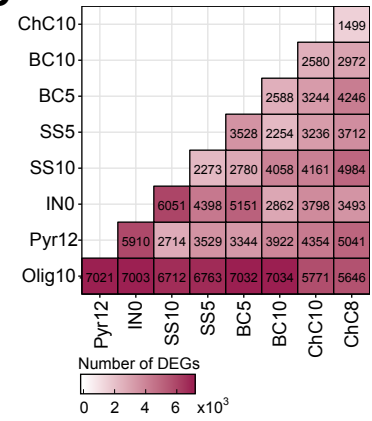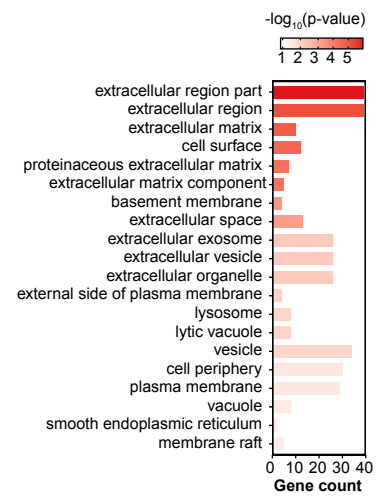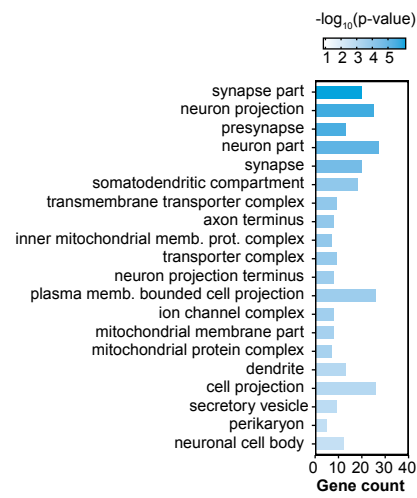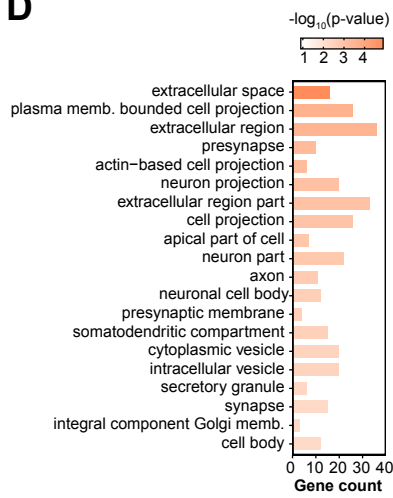
Figure S3

Fig. S3. Further validation of the RNA-seq and gene ontology analysis of interneuron-subtype enriched genes at P10.

(**A**) Analysis of the expression of well-known cell type-specific genes verifies that each cell-type has minimal contamination with other subtypes. (**B**) The expression of well-known synaptogenic genes increases between the selected developmental stages, confirming the suitability of the transcriptome data to identify genes that regulate synapse development. Note that the genes in (B) are also involved in synapse development and exhibit a similar increase in their expression between the two selected stages. (**C**) Heatmap showing the number of differentially expressed genes between cell-types at different stages using a False Discovery Rate (FDR) < 0.05. (**D**) Gene ontology (GO, cellular component category) enrichment analysis performed using the lists of P10 interneuron subtype-specific genes.
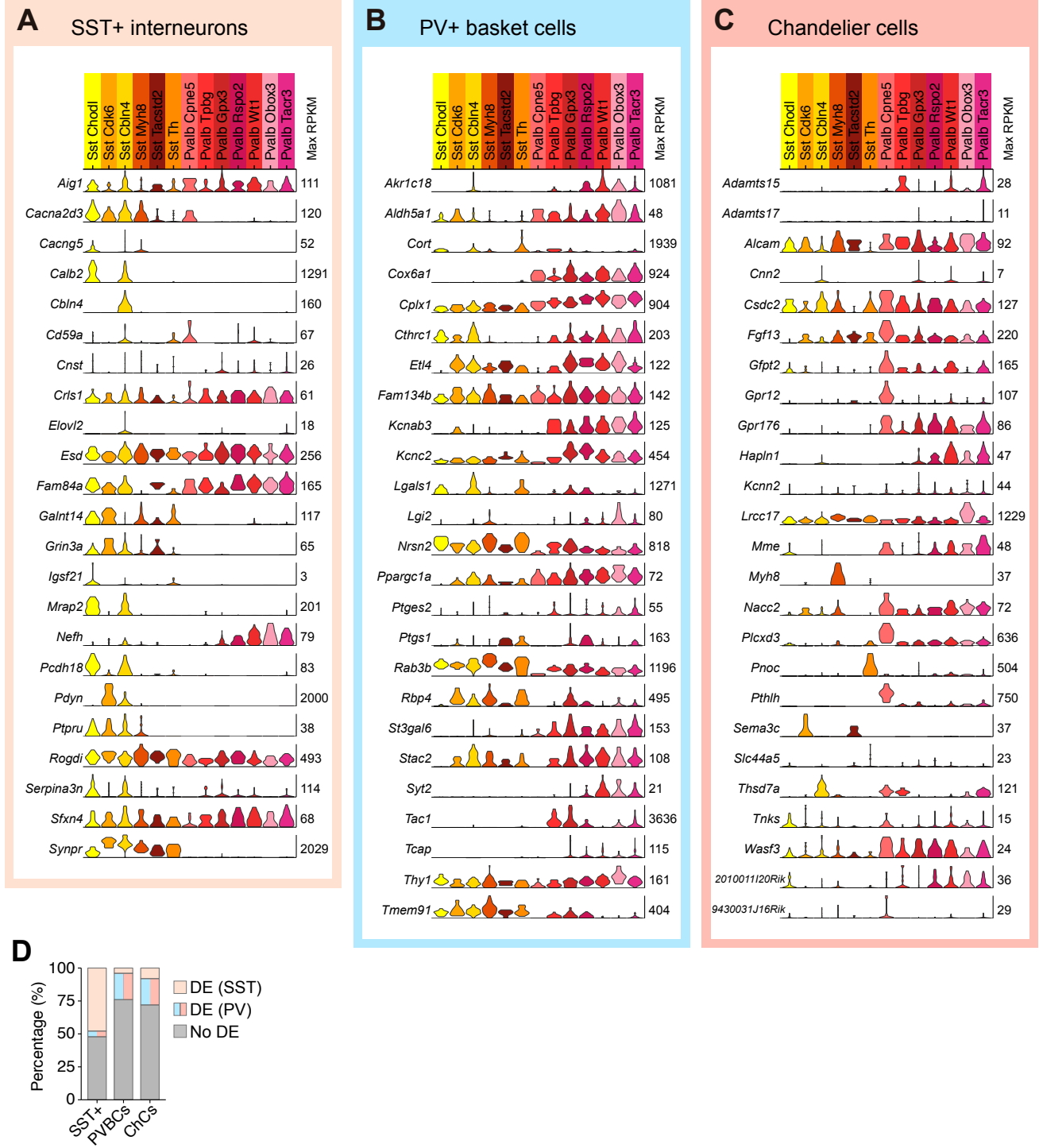
Figure S4

Fig. S4. Expression of interneuron subtype-specific genes during development in adult scRNAseq dataset from Tasic *et al*. 2016 (*1*).

(**A-C**) Violin plots representing the distribution of mRNA expression levels (RPKM) of candidate genes for developing SST+ (A), PV+ basket (B) and chandelier cells (C). Note that genes are displayed in alphabetical order. (**D**) Bar graph illustrating the relative proportion of developmentally-regulated genes that are enriched in the corresponding clusters of SST+ or PV+ cell types identified in Tasic *et al*. 2016 (*1*). The coloured bars follow the colour code for the developing interneuron subtypes. The colours for both basket and chandelier cells are pooled into the genes enriched in PV+ clusters. The grey bars correspond to the percentages of genes in each developing interneuron population that are not enriched in any cell type from the adult dataset.

A SST+ interneurons

	MNC	PVC	CHC	Max RPKM
Aig1				40
Cacna2d3				159
Cacng5				42
Calb2				56
Cbln4				41
Cd59a				18
Cnst				31
Crls1				50
Elovl2				35
Esd				127
Fam84a				35
Galnt14				107
Grin3a				308
Igsf21				12
Mrap2				71
Nefh				150
Pcdh18				90
Ptpru				33
Rogdi				37
Serpina3n				3
Sfxn4				16
Synpr				178

B PV+ basket cells

	MNC	PVC	CHC	Max RPKM
Akr1c18				5
Aldh5a1				96
Cort				67
Cox6a1				72
Cplx1				934
Cthrc1				39
Etl4				311
Fam134b				54
Kcnab3				228
Kcnc2				640
Lgals1				82
Lgi2				35
Nrsn2				46
Ppargc1a				161
Ptges2				34
Ptgs1				31
Rab3b				184
Rbp4				53
St3gal6				22
Stac2				39
Syt2				76
Tac1				546
Tcap				26
Thy1				141
Tmem91				40

C Chandelier cells

	MNC	PVC	CHC	Max RPKM
Adamts15				35
Adamts17				68
Alcam				281
Cnn2				5
Csdc2				14
Fgf13				118
Gfpt2				11
Gpr12				51
Gpr176				130
Hapln1				202
Kcnn2				60
Lrcc17				116
Mme				39
Myh8				53
Nacc2				142
Plcxd3				183
Pnoc				53
Pthlh				169
Sema3c				46
Slc44a5				156
Thsd7a				428
Tnks				25
Wasf3				20

D

Percentage (%)

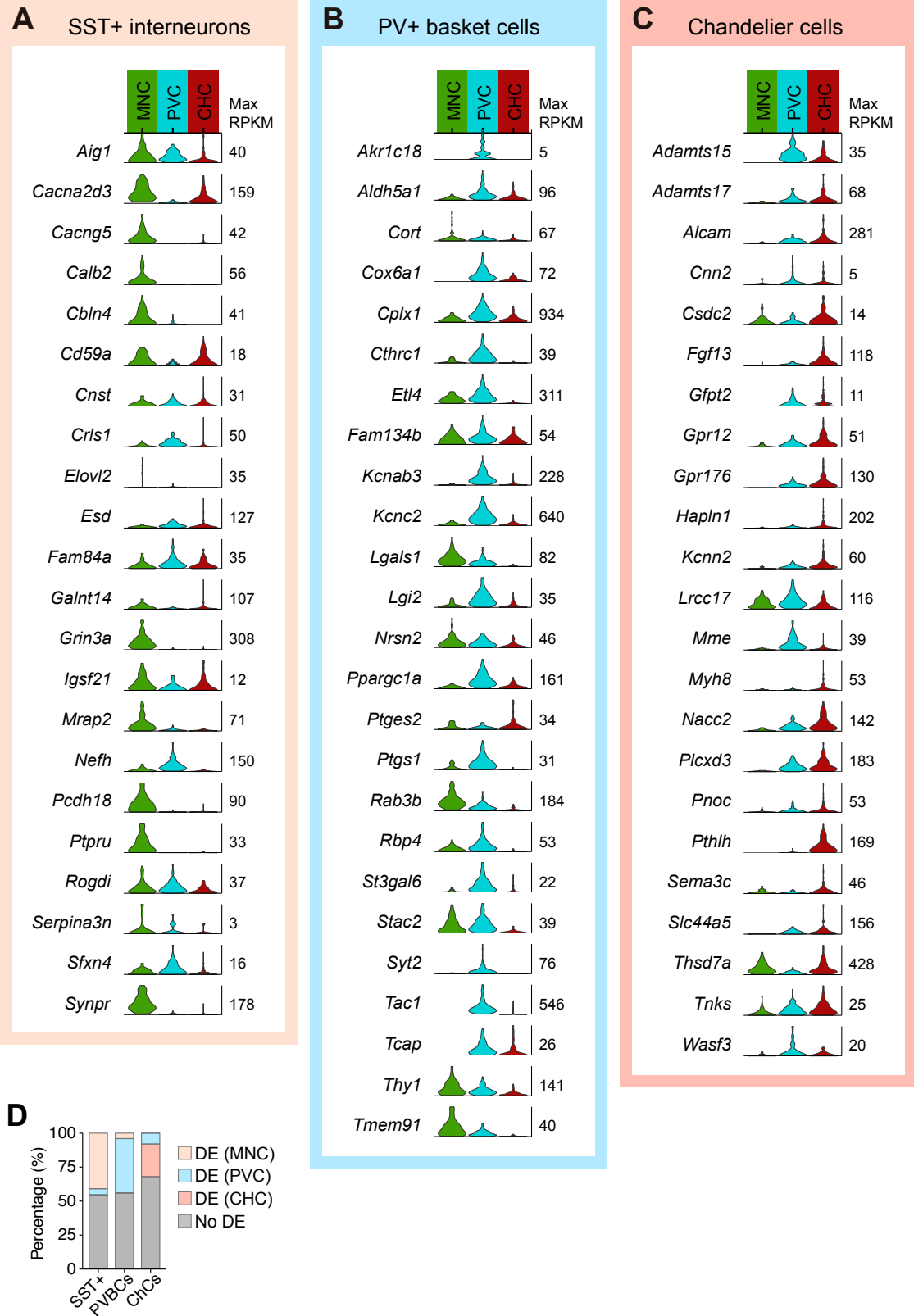- DE (MNC)
- DE (PVC)
- DE (CHC)
- No DE

SST+ PVBCs ChCs

Figure S5

Fig. S5. Expression of interneuron subtype-specific genes during development in adult scRNAseq dataset from Paul *et al*. 2017 (*6*).
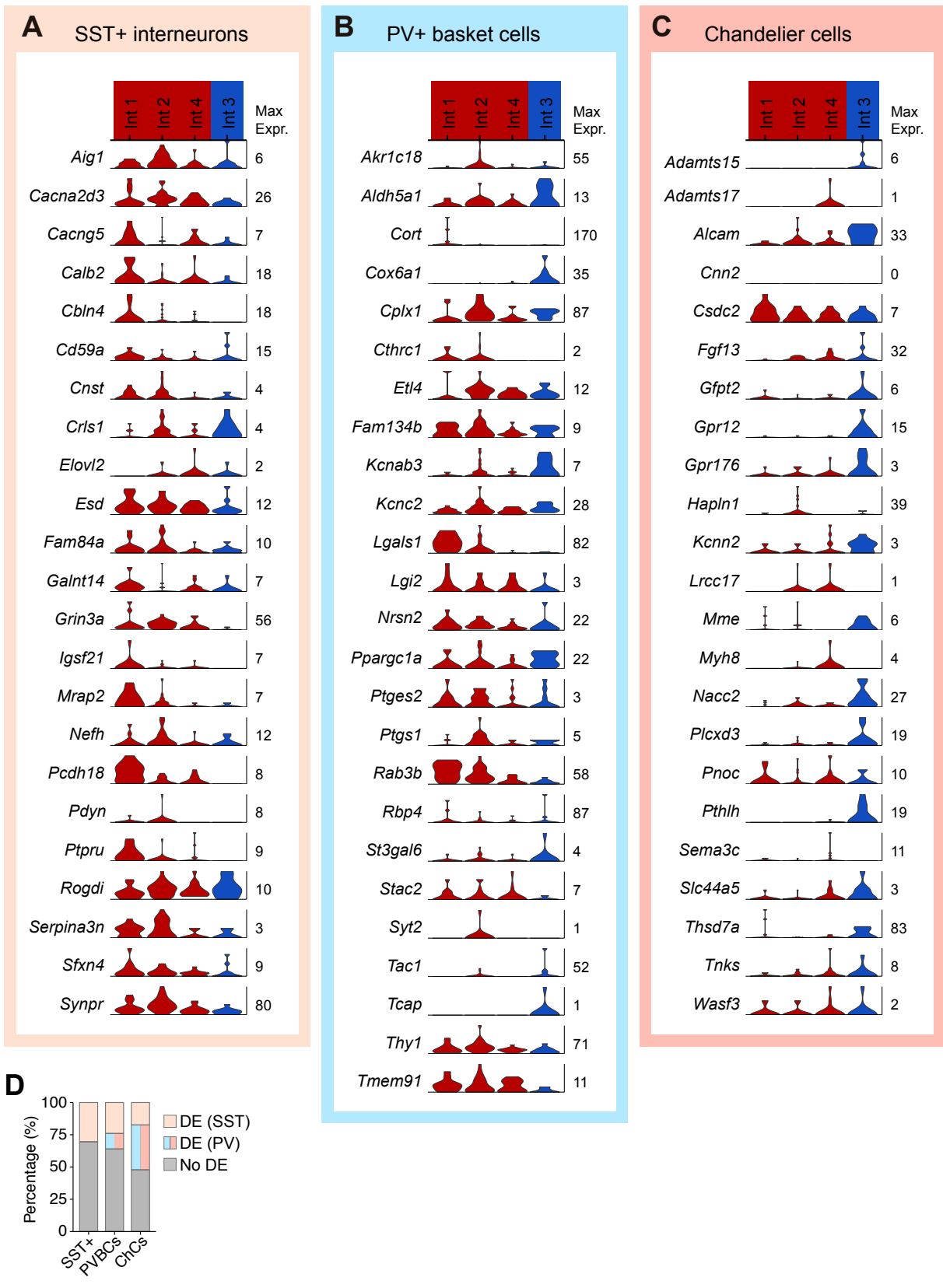
(**A-C**) Violin plots representing the distribution of mRNA expression levels (RPKM) of candidate genes for developing SST+ (A), PV+ basket (B) and chandelier cells (C). Note that genes are displayed in alphabetical order. (**D**) Bar graph illustrating the relative proportion of developmentally-regulated genes that are enriched in the corresponding cell types–Martinotti cells (MNC), PV+ basket cells (PVC), and chandelier cells (CHC)– sorted in Paul *et al*. 2017 (*6*). The coloured bars follow the colour code for the developing interneuron subtypes. The grey bars correspond to the percentages of genes in each developing interneuron population that are not enriched in any cell type from the adult dataset.

Figure S6

Fig. S6. Expression of interneuron subtype-specific genes during development in adult scRNAseq dataset from Zeisel *et al*. 2015 (*5*).

(**A-C**) Violin plots representing the distribution of mRNA expression levels (molecules/cell) of candidate genes for developing SST+ (A), PV+ basket (B) and chandelier cells (C). Note that genes are displayed in alphabetical order. (**D**) Bar graph illustrating the relative proportion of developmentally-regulated genes that are enriched in the corresponding clusters of SST+ or PV+ cell types identified in Zeisel *et al*. 2015 (*5*). The coloured bars follow the colour code for the developing interneuron subtypes. The colours for both basket and chandelier cells are pooled into the genes enriched in the PV+ clusters (Int. 3). The grey bars correspond to the percentages of genes in each developing interneuron population that are not enriched in any cell type from the adult dataset.
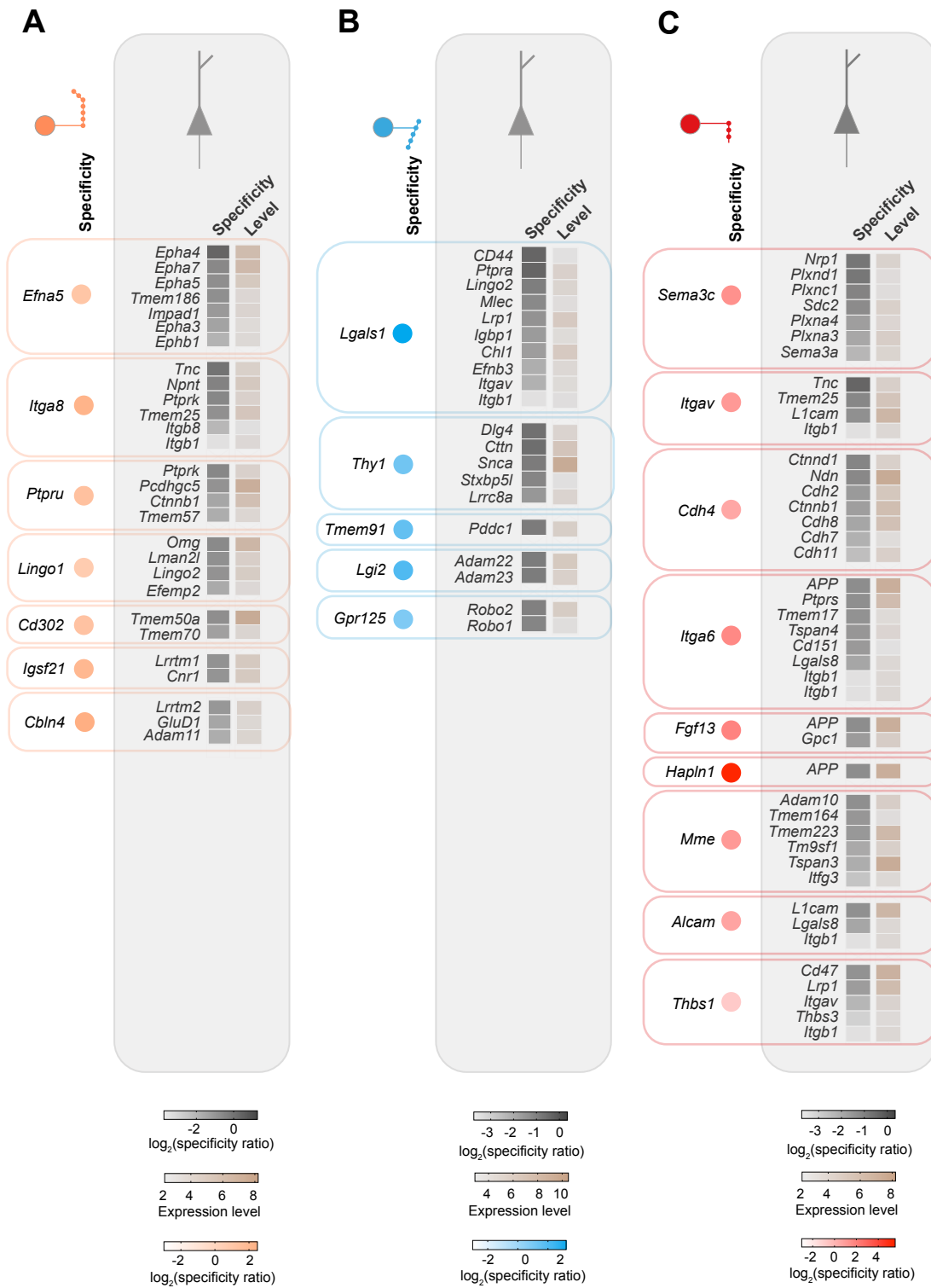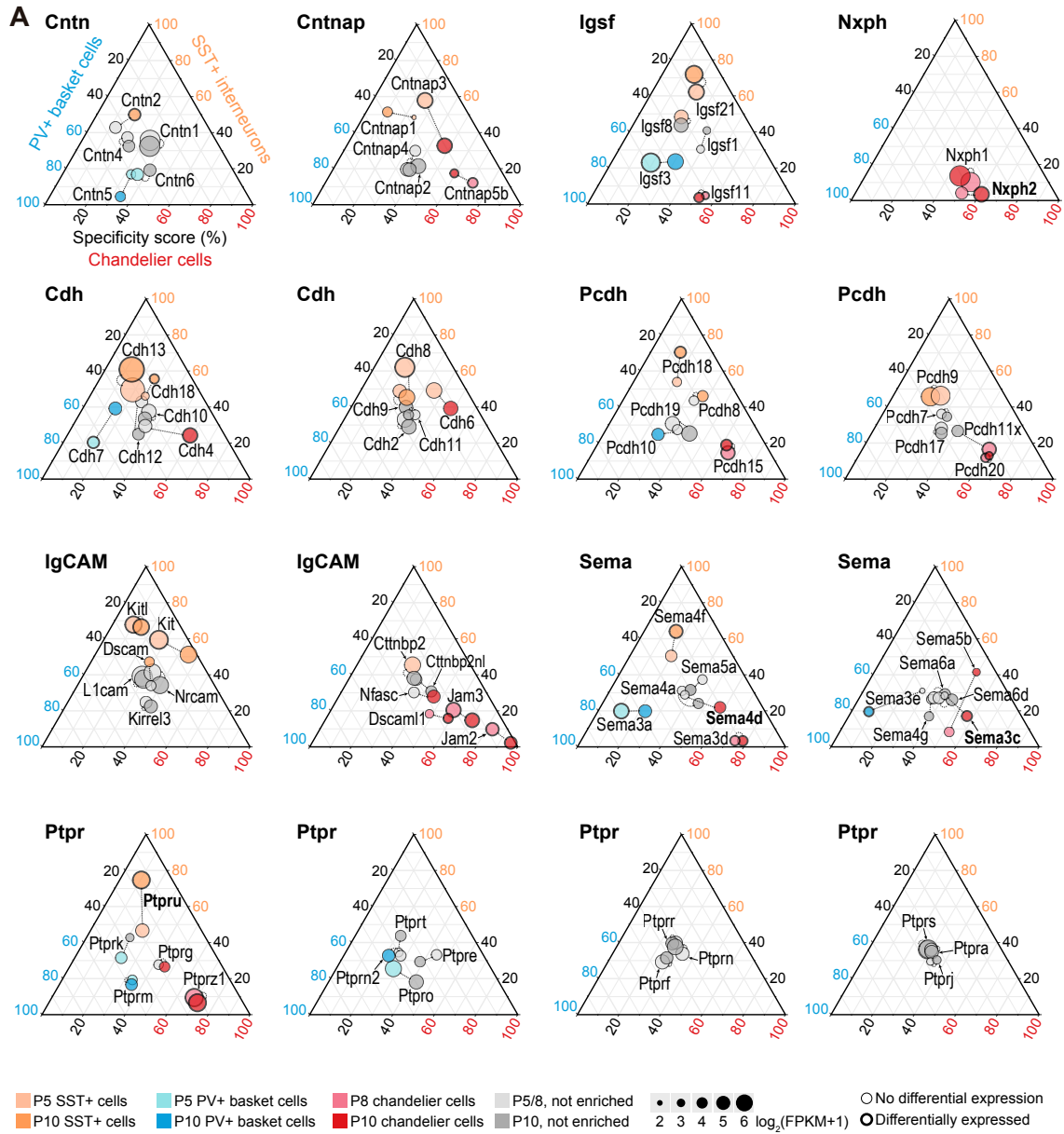
Figure S7

Fig. S7. Matching interneuron subtype-specific and pyramidal cell gene/protein-pairs.

(A-C) Cell-specific candidate synaptic molecules expressed in SST+ (A), PV+ basket (B) and chandelier cells (C) ranked based on the presence and specificity of their putative postsynaptic partners in pyramidal neurons (see Table S4 for details). Note that this analysis relies on known protein-protein interactions and, therefore, proteins for which a partner has not yet been identified have an artificially biased lower ranking.
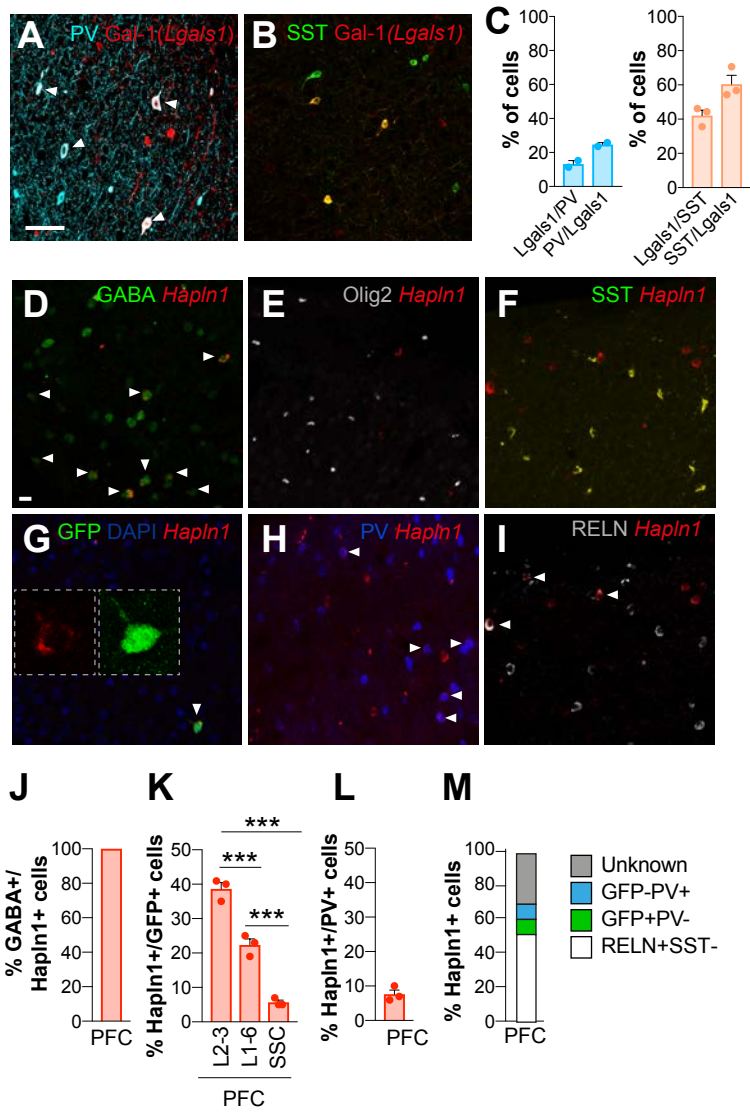
Figure S8

Fig. S8. Differential gene expression and dynamics of protein families related to synapse formation and function in different interneuron subtypes.

(A) Ternary diagrams for different protein families: contactins (Cntn), contactin-associated proteins (Cntnap), immunoglobulin superfamily members (Igsf), cadherins (Cdh), non-clustered protocadherins (Pcdh), immunoglobulin-like cell adhesion molecules (IgCAM), semaphorins (Sema) and protein tyrosine phosphatase receptors (PTPR). The dot size corresponds to the maximum level of expression of each gene ($\log_2$FPKM+1) in the three subpopulations at P5/8 or P10. Differentially expressed genes are represented with solid outlines (FDR < 0.05). Enriched genes are color-coded for a particular interneuron population based on the cell type specificity score (>0.45). Gray colors were used for genes that did not show enrichment for any interneuron subtype. Genes highlighted in bold showed a 2-fold or higher upregulation in their expression levels (FPKM) between both developmental stages.

Figure S9

Fig. S9. Characterization of *Lgals1* and *Hapln1* expression.

(**A-B**) Representative image showing the colocalization of Lgals1 with PV and SST. SST cells were fated-mapped and labeled using *SST$^{Cre/+}$;RCE*. Scale bars equal to 50 μm. (**C**) Percentage of PV+ cells that express *Lgals1* and of *Lgals1+* cells that express PV. Percentage of SST+ cells that express *Lgals1* and of *Lgals1+* cells that express SST. (**D-I**) Representative images showing the colocalization of *Hapln1* mRNA with GABA, Olig2, SST, chandelier cells (*Nkx2-1$^{CreER/+}$;RCE*), PV and Reelin at P30 in the mouse prefrontal cortex (PFC). Scale bars equal to 20 μm. (**J**) Percentage of *Hapln1+* cells that express GABA at P30 in the mouse prefrontal cortex (PFC, n = 3 mice). Note that all *Hapln1+* cells are GABAergic. (**K**) Percentage of chandelier cells in the indicated regions/layers (labeled upon P2 Tamoxifen induction in *Nkx2-1$^{CreER/+}$RCE* mice) that express *Hapln1* at P30 (n = 3 mice). Note the increase in the percentage of colocalizing cells in layers/regions enriched in chandelier cells. One-way ANOVA (p<0.001), followed by Holm Sidak's multiple comparisons test (p<0.001 for all comparisons). (**L**) Fraction of PV+ cells that express *Hapln1* in the prefrontal cortex at P30 (n = 3 mice). Note the low colocalization, consistent with expression in some PV+ chandelier but not basket cells. (**M**) Identification of cell types expressing *Hapln1* in the prefrontal cortex (PFC) at P30 (n = 3 mice per condition). GFP+ cells (both PV+ and PV-) are labeled chandelier cells and RELN+SST- cells are neurogliaform cells.
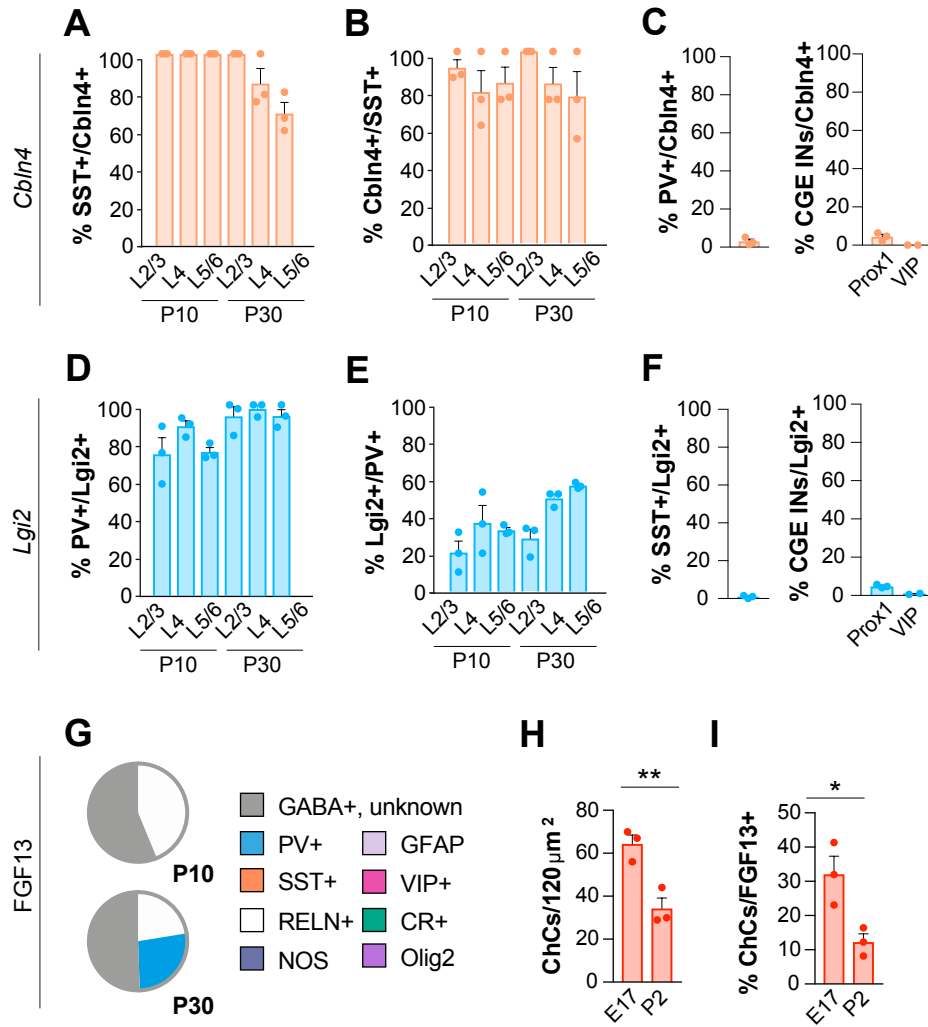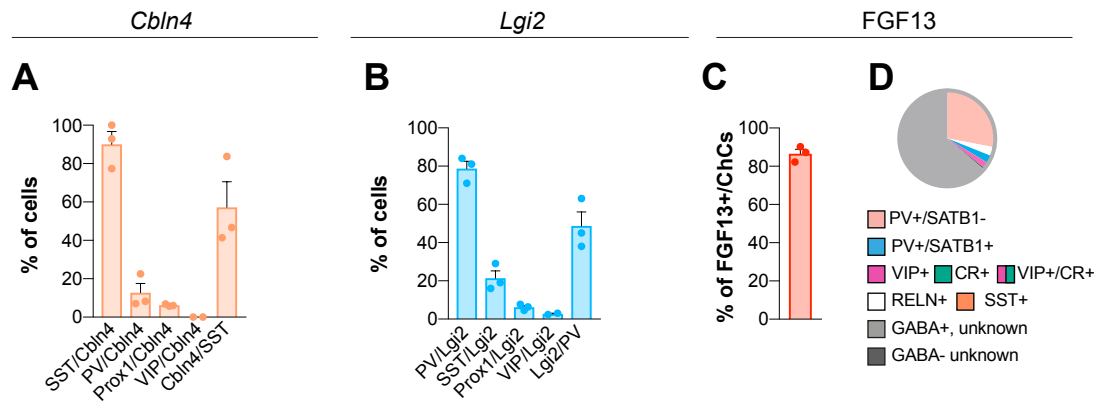
Figure S10

Fig. S10. Characterization of *Cbln4*, *Lgi2* and *Fgf13* expression in interneuron subtypes during development.

(**A**) Percentage of *Cbln4*+ cells (detected by in situ hybridization) that express SST in the indicated layers of the mouse somatosensory cortex at P10 and P30. (**B**) Percentage of SST+ cells that express *Cbln4* in the indicated layers of the mouse somatosensory cortex at P10 and P30. (**C**) Percentage of *Cbln4*+ cells that express PV at P30 (left bar graph) and percentage of *Cbln4*+ cells that are Prox1+ (fate-mapped using *Dlx6a$^{Cre/+}$;Prox1-eGFP$^{+/F}$* mice and analyzed at P60) or VIP+ (fate-mapped using *VIP$^{Cre/+}$;RCE* mice and analyzed at P25) interneurons derived from the caudal ganglionic eminence (CGE INs, right bar graph). (**D**) Percentage of *Lgi2*+ cells (detected by in situ hybridization) that are PV+ in the indicated layers of the mouse somatosensory cortex at P10 (*Lhx6Cre;RCE*+SST- cells) and P30 (PV+ cells). (**E**) Percentage of PV+ cells that express *Lgi2* in the indicated layers of the mouse somatosensory cortex at P10 (*Lhx6Cre;RCE*+SST- cells) and P30 (PV+ cells). (**F**) Percentage of *Lgi2*+ cells that express SST at P30 (left bar graph) and percentage of *Lgi2*+ cells that are Prox1+ (fate-mapped using *Dlx6a$^{Cre/+}$;Prox1-eGFP$^{+/F}$* mice and analyzed at P60) or VIP+ (fate-mapped using *VIP$^{Cre/+}$;RCE* mice and analyzed at P25) interneurons derived from the caudal ganglionic eminence (CGE INs, right bar graph). (**G**) Analysis of the identity of FGF13+ cells by colocalizing FGF13 with different markers at P10 and P30 in the mouse prefrontal cortex. All FGF13+ cells are GABAergic but they are negative for all markers except Reelin and PV (note that the colocalization with PV could not be assessed at P10 due to its late expression). This analysis, together with the observation that all labeled chandelier cells express FGF13 (Fig. 2E), is the base for the estimation provided in Figure 2E ("ChCs est" are FGF13+GABA+Reelin- bottom graph). (**H**) Density of chandelier cells in layer II/III of the mouse prefrontal cortex at P30 upon Tamoxifen induction at E17 or P2. Note that significantly more chandelier cells are labeled by embryonic induction. **$p<0.01$, Student t-test. (**I**) Fraction of FGF13+ cells in layer II/III that are chandelier cells at P30 upon Tamoxifen induction at E17 or P2. Note that the percentage of FGF13+ cells that are chandelier cells is significantly higher upon embryonic induction. *$p<0.05$, Student t-test. Based on the data from (H) and (I), GABAergic cells that are not positive for any known marker are likely chandelier cells that are not labeled by the Tamoxifen induction.

Figure S11

Fig. S11. Expression of *Cbln4*, *Lgi2* and FGF13 in the hippocampus.

(**A**) Percentage of *Cbln4*+ cells (detected by in situ hybridization) that express SST, PV, Prox1 or VIP in the mouse hippocampus (ages and labeling strategies as in figure S10). Note that SST+PV+ cells are included in the SST/Cbln4 bar. Percentage of SST+ cells that express *Cbln4* in the mouse hippocampus at P30 (right). (**B**) Percentage of *Lgi2*+ cells (detected by in situ hybridization) that express PV, SST, Prox1 or VIP in the mouse hippocampus (ages and labeling strategies as in figure S10). Note that SST+PV+ cells are included in the PV/Lgi2 bar. Percentage of PV+ cells that express *Lgi2* in the mouse hippocampus at P30 (right). (**C**) Percentage of chandelier cells (PV+/SATB1-, as reported by (*59*)) that are FGF13+ in the mouse hippocampus at P30. (**D**) Analysis of the identity of FGF13+ cells in the mouse hippocampus at P30 by colocalizing FGF13 with different markers. All FGF13+ cells are GABAergic and a large proportion (~30%) are PV+ chandelier cells (PV+/SATB1-). Few FGF13+ cells are Reelin+ (3%), PV+/SATB1+ (2.6%) and VIP+ (2.1%).

Figure S12
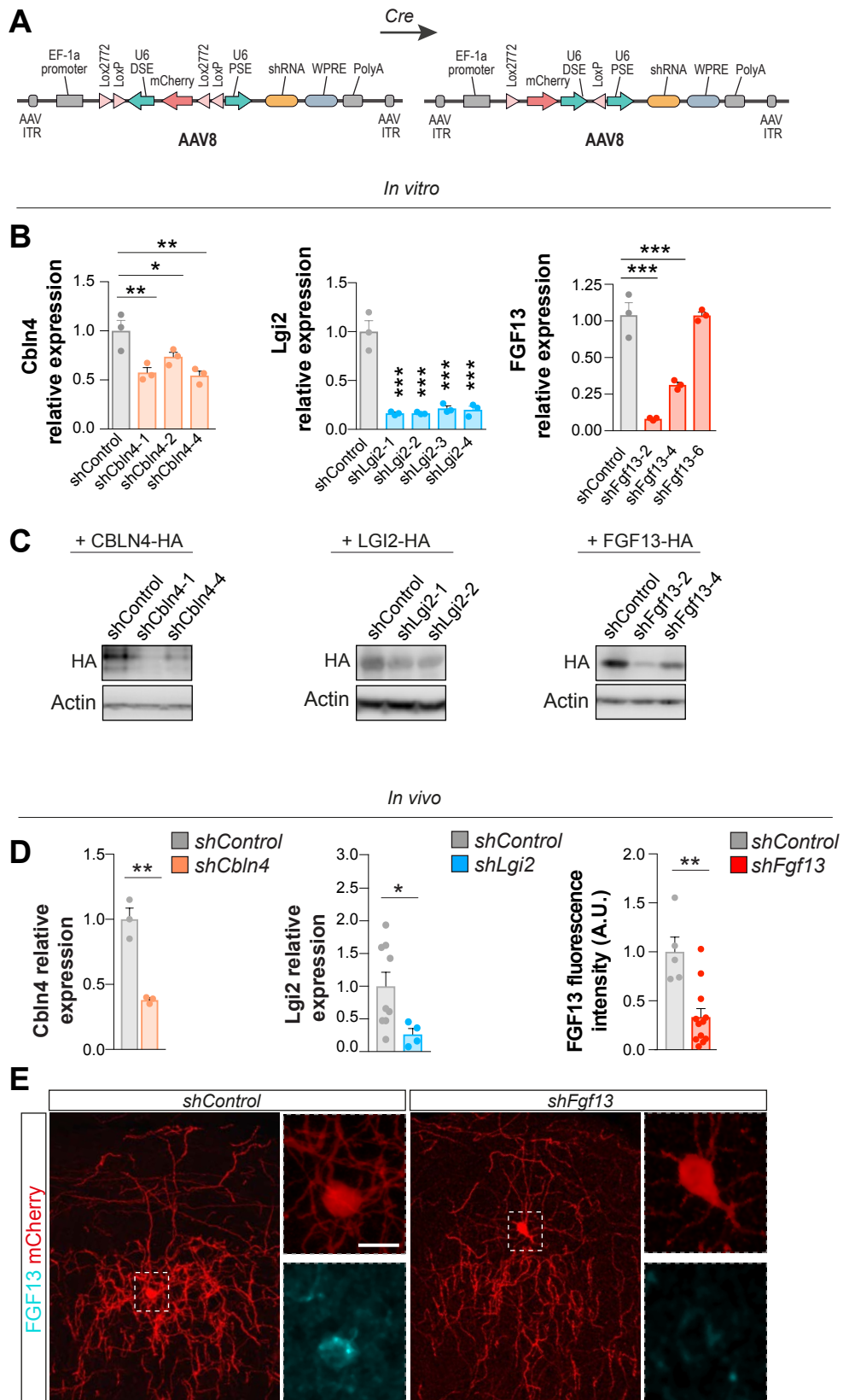
Fig. S12. *In vitro* and *in vivo* validation of the downregulation efficiency.

(**A**) Map of the viral Cre-dependent constructs expressing mCherry and the miR-based shRNAs used for the knock-down experiments. (**B**) *Cbln4, Lgi2* and *Fgf13* mRNA expression assessed by qPCR (as expression relative to control) upon co-transfection of HEK cells with the expression plasmids for the different HA-tagged proteins and corresponding shRNAs (n = 3 wells). *p<0.05, **p<0.01, ***p<0.001, One-way ANOVA followed by Holm-Sidak's multiple comparisons test. (**C**) CBLN4-HA, LGI2-HA and FGF13-HA *in vitro* protein expression assessed by Western Blot upon downregulation using the shRNAs selected for the *in vivo* experiments. (**D**) *Cbln4* (*shCbln4*, n = 3 mice, control, n = 3 mice) and *Lgi2* (*shLgi2*, n = 4 mice; control, n= 9 mice injected with the control virus) mRNA expression levels assessed by qPCR (as expression relative to the control) on the infected mouse brain tissue 25 days after injection of the corresponding AAVs. FGF13 protein intensity (expressed as relative to the control; *shFgf13,* n = 12 cells from 5 mice; control, n = 5 cells from 3 mice) assessed by IHC upon *in vivo* downregulation. *p<0.05, ***p<0.001, Student t-test. (**E**) Representative images (maximum projection from a confocal z-stack) showing mCherry+ chandelier cells from sparse viral infection. FGF13 immunoreactivity in mCherry+ chandelier cells was observed only in control cells but not cells expressing *shFgf13*. Scale bars equal 20 μm.
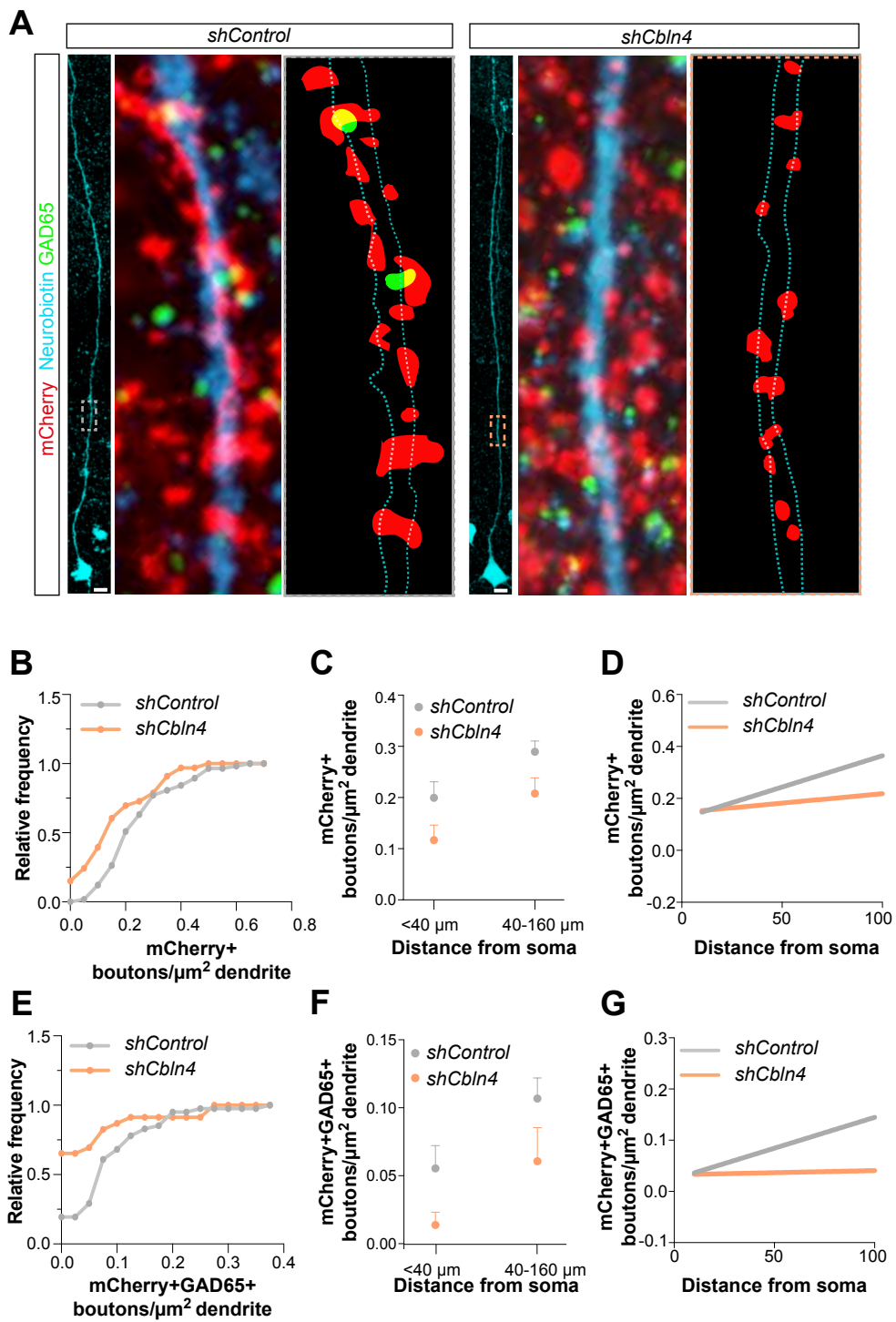
Figure S13

Fig. S13. Decrease of SST+ presynaptic terminals contacting the proximal and distal dendrites of pyramidal neurons in absence of *Cbln4*.

(**A**) Representative images showing the dendrites of neurobiotin-filled pyramidal neurons in *SST-Cre* mice injected at P3 with control or *shCbln4*-expressing virus and analyzed at P30-40. The insets (raw images and masks) are showing mCherry+GAD65+ presynaptic boutons contacting the highlighted portions of the distal dendrites. Scale bars equal 10 μm. (**B**) Cumulative probability plots for mCherry contact density onto 10 μm-long segments of dendrite (total length analyzed: 0-100 μm from the soma) in *SST-Cre* mice injected with control (n = 57 segments from 4 cells, 3 mice) or *shCbln4*-expressing (n = 33 segments from 3 cells, 3 mice). Kolmogorov-Smirnov test, p = 0.0051. (**C**) mCherry average contact density onto 10 μm-long segments of proximal (total length analyzed: 0-40 μm from the soma) or distal (total length analyzed: 40-160 μm from the soma) dendrites in *SST-Cre* mice injected with control (n = 16 proximal and 40 distal dendritic segments from 4 cells, 3 mice) or *shCbln4*-expressing (n = 12 proximal and 21 distal dendritic segments from 3 cells, 3 mice). Two-way ANOVA, control vs *shCbln4* p = 0.0086, proximal vs distal p = 0.0039, interaction p = 0.9879. Sidak's multiple comparisons: control vs *shCbln4* in proximal dendrite p = 0.1924, control vs *shCbln4* in distal dendrite p = 0.0449, control in proximal vs distal dendrite p = 0.0435, *shCbln4* in proximal vs distal dendrite p = 0.1114 (**D**) Linear regression lines of mCherry+ contact density onto 10 μm-long consecutive dendritic segments (total length analyzed: 0-100 μm from the soma) in *SST-Cre* mice injected with control (n = 4 cells from 3 mice/segment) or *shCbln4*-expressing (n = 3 cells from 3 mice/segment). Linear regression analysis, p = 0.2458, showing that the differences between the slopes are not significant. (**E**) Cumulative probability plots for mCherry+GAD65+ presynaptic bouton density onto 10 μm-long segments of dendrite (total length analyzed: 0-100 μm from the soma) in *SST-Cre* mice injected with control (n = 41 segments from 3 cells, 3 mice) or *shCbln4*-expressing (n = 23 segments from 2 cells, 2 mice). Kolmogorov-Smirnov test, p = 0.0012. (**F**) mCherry+GAD65+ average presynaptic bouton density onto 10 μm-long segments of proximal (total length analyzed: 0-40 μm from the soma) or distal (total length analyzed: 40-160 μm from the soma) dendrites in *SST-Cre* mice injected with control (n = 12 proximal and 29 distal dendritic segments from 3 cells, 3 mice) or *shCbln4*-expressing (n = 8 proximal and 15 distal dendritic segments from 2 cells, 2 mice). Two-way ANOVA, control vs *shCbln4* p = 0.0456, proximal vs distal p = 0.0260, interaction p = 0.9165. Sidak's multiple comparisons: control vs *shCbln4* in proximal dendrite p = 0.4266, control vs *shCbln4* in distal dendrite p = 0.1264, control in proximal vs distal dendrite p = 0.1121, *shCbln4* in proximal vs distal dendrite p = 0.3139. (**G**) Linear regression lines of mCherry+GAD65+ presynaptic bouton density onto 10 μm-long consecutive dendritic segments (total length analyzed: 0-100 μm from the soma) in *SST-Cre* mice injected with control (n = 3 cells from 3 mice/segment) or *shCbln4*-expressing (n = 2 cells from 2 mice/segment). Linear regression analysis, p = 0.1400, showing that the differences between the slopes are not significant.
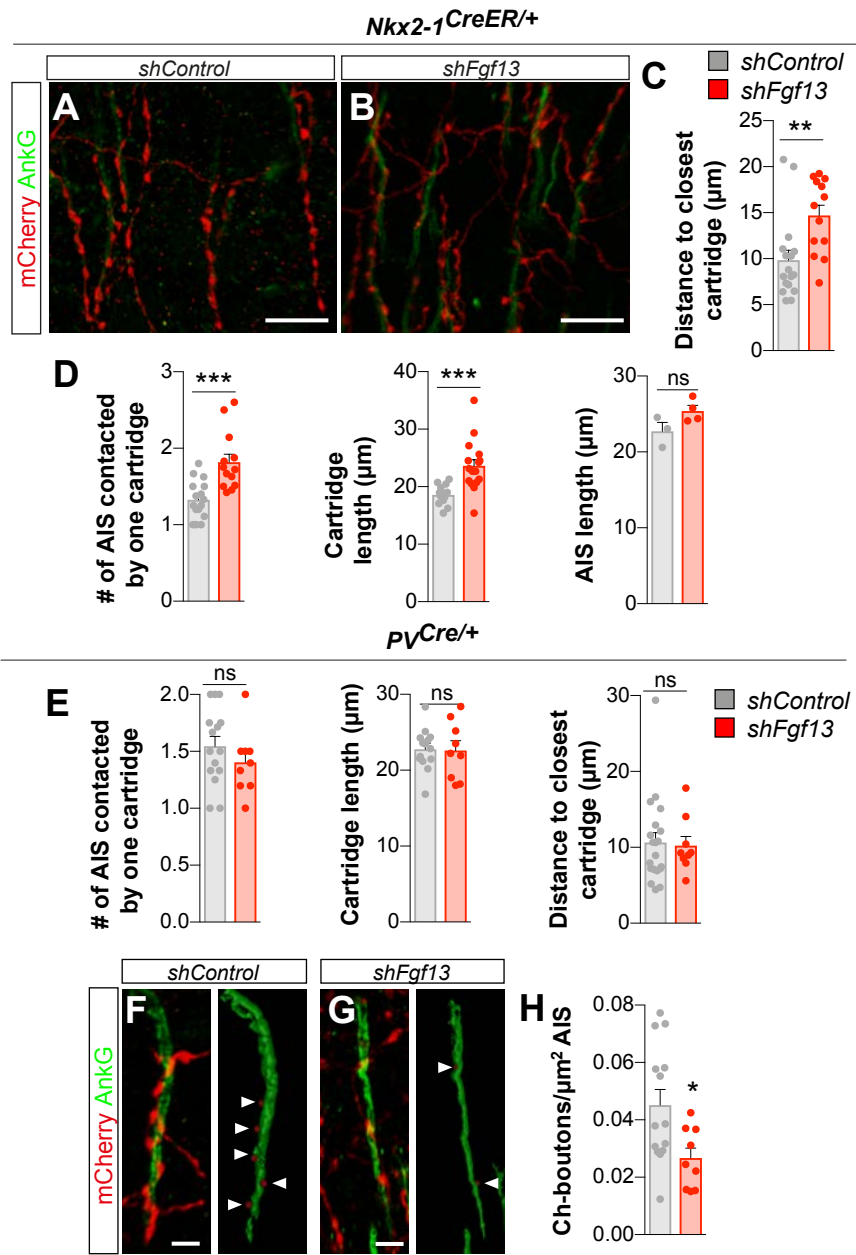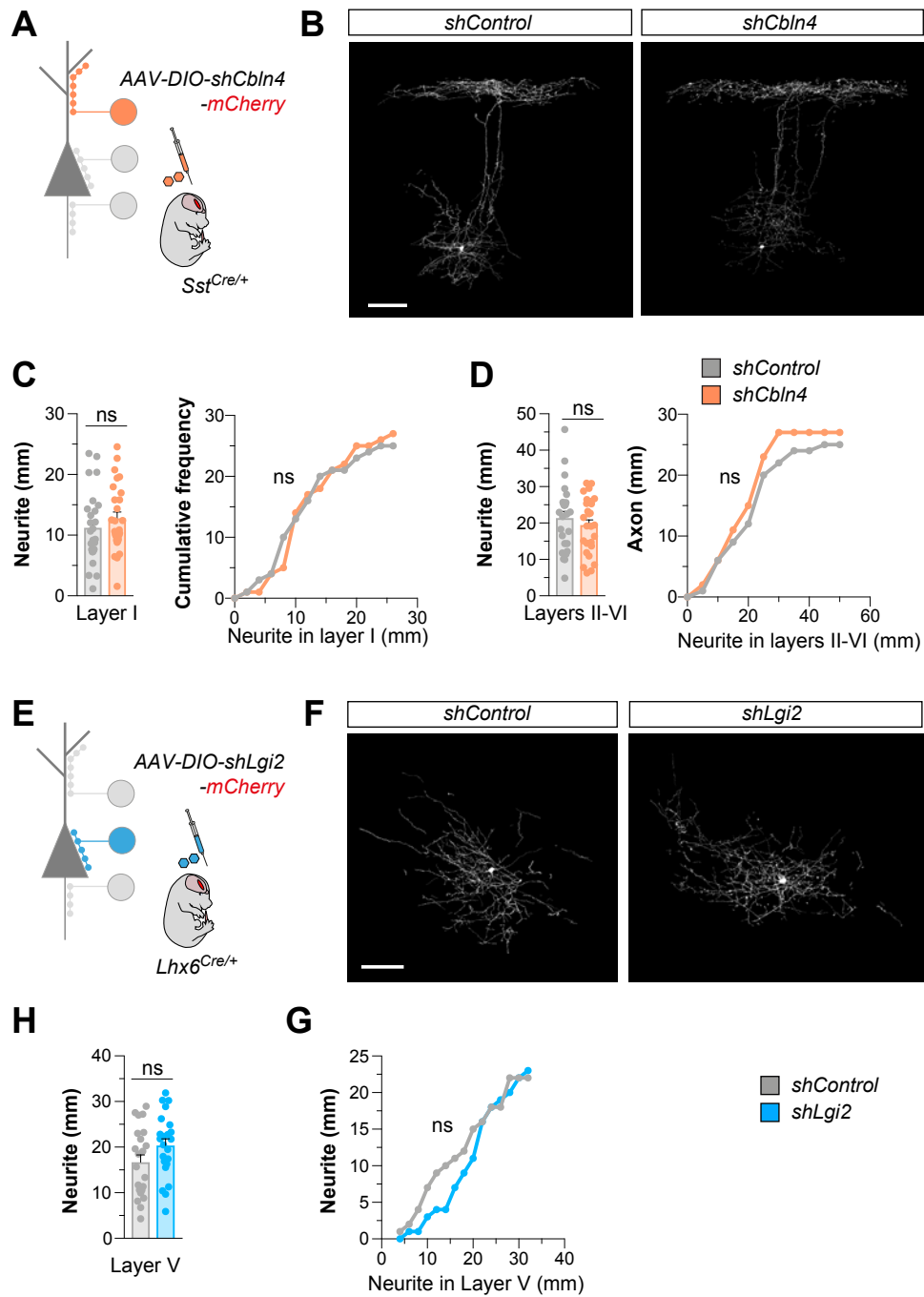
Figure S14

Fig. S14. Disorganization of the chandelier cell arbor upon early but not late loss of *Fgf13*.
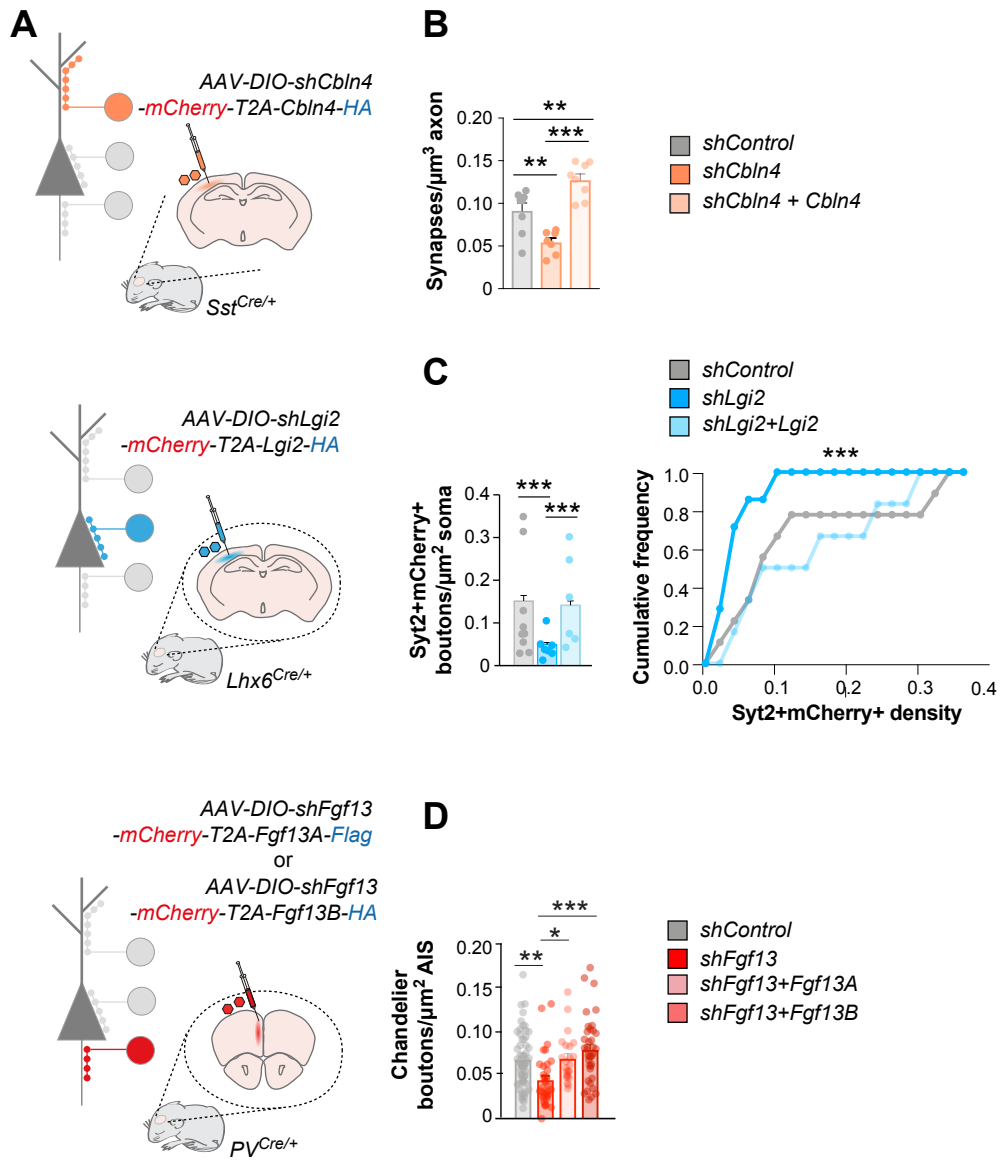
(**A** and **B**) Representative images showing sparser arborization and disorganization of chandelier axons at P30 in FGF13 knock-down cells (**B**) compared to control cells infected with a control virus (**A**). Scale bars equal 10 μm. (**C**) Quantification of the 'distance to closest cartridge' (measured as the average distance between each cartridge and the cartridge that is closest to it and used as a proxy to estimate the density of the chandelier arbor) in FGF13 knock-down cells (n = 17 cells from 3 mice) compared to controls (n = 13 cells from 3 mice). **p<0.01, Mann Whitney test. (**D**) Quantification of the number of axon initial segments contacted by one cartridge in FGF13 knock-down cells (n = 16 cells from 3 mice) compared to controls (n = 13 cells from 3 mice). ***p<0.001, Mann Whitney test. Quantification of the average cartridge length in FGF13 knock-down cells (n = 14 cells from 3 mice) compared to controls (n = 16 cells from 3 mice). ***p<0.001, Student t-test. Quantification of the average AIS length in *shFgf13* injected mice (n = 3 mice) compared to controls (n = 4 mice). ns, Student t-test. (**E**) Quantification of the number of axon initial segments contacted by one cartridge in FGF13 knock-down cells (n = 9 cells from 5 *PV^{Cre/+}* mice) compared to controls (n = 15 cells from 5 *PV^{Cre/+}* mice). ns, Student t-test. Quantification of the average cartridge length in FGF13 knock-down cells (n = 9 cells from 5 *PV^{Cre/+}* mice) compared to controls (n = 14 cells from 5 *PV^{Cre/+}* mice). ns, Student t-test. Quantification of the 'distance to closest cartridge' in FGF13 knock-down cells (n = 9 cells from 5 *PV^{Cre/+}* mice) compared to controls (n = 20 cells from 5 *PV^{Cre/+}* mice). **p<0.01, Mann Whitney test. (**F** and **G**) Representative images and Imaris reconstruction showing the reduced density of chandelier presynaptic boutons contacting the axon initial segment in *PV^{Cre/+}* mice infected with control or *shFgf13*-expressing virus. Scale bar equal 3 μm. (**H**) Quantification of the average density of mCherry+ synapses per surface unit of axon initial segment (AnkG) made by chandelier cells in *PV^{Cre/+}* mice infected with control (n = 14 cells from 5 mice) or *shFgf13*-expressing virus (n = 9 cells from 5 mice). *p<0.05, Student t-test.

Figure S15

Fig. S15. Normal axonal morphology in SST+ cells expressing *shCbln4* and PV+ cells expressing *shLgi2*.

(**A**) Schematic of AAV in utero injections in E14.5 *SST-Cre* mice. (**B**) Representative images showing the morphology of control and *shCbln4*-expressing Martinotti cells from layer V of the somatosensory cortex at P21. (**C, D**) Quantification of the total axonal length and cumulative frequency plots for the length of Martinotti cell axons in layer I (**C**) and layers II/III (**D**) (n = 25 neurons from 8 mice, *shControl,* n = 27 neurons from 5 mice, *shCbln4*). No significant differences, Student t-test. (**E**) Schematic of AAV in utero injections in E15.5 *Lhx6^{Cre/+}* mice. Representative images showing the morphology of control and *shLgi2*-expressing PV+ basket cells from layer V of somatosensory cortex at P21. (**F**) Quantification of the total axonal length and cumulative frequency plots for the length of PV+ basket cell axons in layer V (n = 22 neurons from 5 mice, *shControl,* n = 23 neurons from 4 mice, *shLgi2*). No significant differences, Student t-test.

A

AAV-DIO-shCbln4
-mCherry-T2A-Cbln4-HA

Sst$^{Cre/+}$

B

Synapses/µm³ axon

- *shControl*
- *shCbln4*
- *shCbln4 + Cbln4*

**

***

**

AAV-DIO-shLgi2
-mCherry-T2A-Lgi2-HA

Lhx6$^{Cre/+}$

C

Syt2+mCherry+ boutons/µm² soma

***
***

- *shControl*
- *shLgi2*
- *shLgi2+Lgi2*

Cumulative frequency

Syt2+mCherry+ density

***

AAV-DIO-shFgf13
-mCherry-T2A-Fgf13A-Flag
or
AAV-DIO-shFgf13
-mCherry-T2A-Fgf13B-HA

PV$^{Cre/+}$

D

Chandelier boutons/µm² AIS

**
*
***

- *shControl*
- *shFgf13*
- *shFgf13+Fgf13A*
- *shFgf13+Fgf13B*

Figure S16

Fig. S16. *In vivo* rescue of the downregulated genes confirms the specificity of the synaptic phenotype.

(**A**) Schematic of AAV injections at P2-P3 in the indicated regions analyzed at P30 and Cre-expressing mice. (**B**) Quantification of GAD65+ boutons inside the mCherry+ axons of SST+ cells contacting Gephyrin+ postsynaptic clusters in layer I of the somatosensory cortex of *SST-Cre* mice injected at P3 with control (n = 8 mice, same data as in Fig. 3C) or *shCbln4-* (n = 8 mice, same data as in Fig. 3C) or *Cbln4-*HA expressing virus (n = 8 mice). **p<0.01, Kruskal-Wallis test followed by Holm-Sidak's multiple comparisons test. (**C**) Quantification of mCherry+Syt2+ somatic synapses per surface unit of pyramidal cell soma in *Lhx6$^{Cre/+}$* mice injected at P3 with control (n = 6 mice, same data as in figure 3E) or *shLgi2-* (n = 7 mice, same data as in figure 3E) or *Lgi2-*HA expressing virus (n = 9 mice). ***p<0.01, Kruskal-Wallis test. (**D**) Quantification of mCherry+ synapses per surface unit of axon initial segment (AnkG) made by *PV$^{Cre/+}$* chandelier cells infected at P2 with control (n = 58 AIS from 8 mice), *shFgf13-* (n = 35 AIS from 6 mice), *Fgf13A-*Flag (n = 21 AIS from 6 mice) or *Fgf13B-*HA expressing virus (n = 38 AIS from 6 mice, *mFgf13B*). *p<0.05, **p<0.01, ***p<0.001, Kruskal-Wallis test.
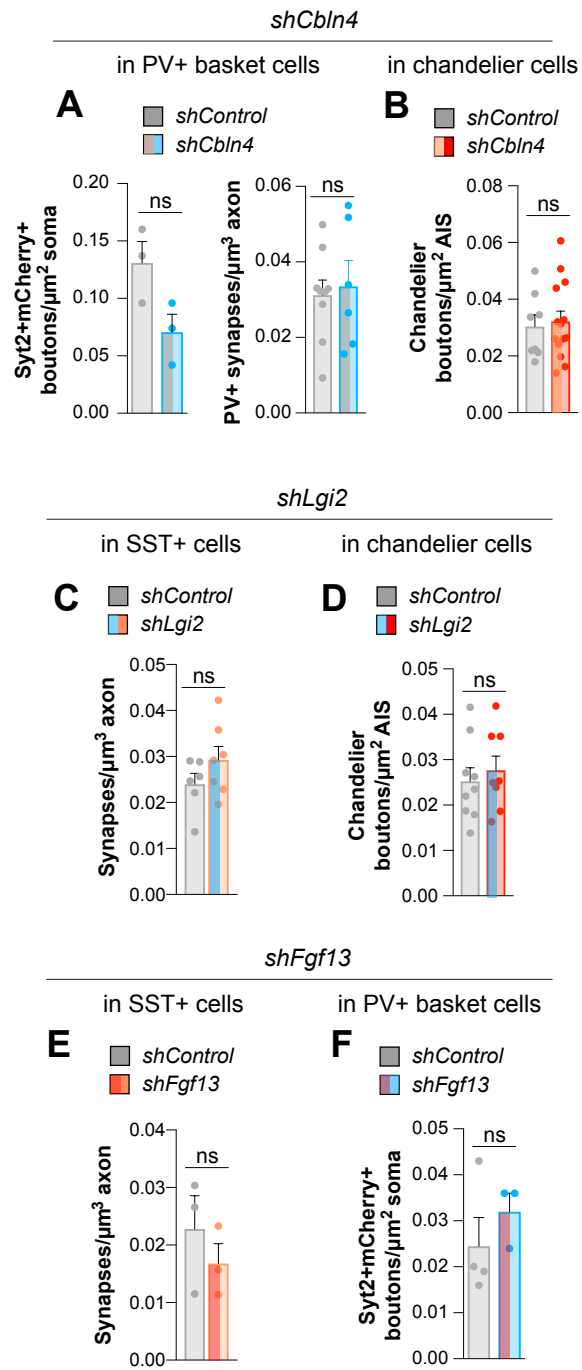
Figure S17

Fig. S17. Downregulation of *Cbln4*, *Lgi2* and *Fgf13* does not affect synapse formation in other interneuron subtypes.

(**A**) *Left:* quantification of mCherry+Syt2+ somatic synapses per surface unit of pyramidal cell soma in *Lhx6^{Cre/+}* mice injected at P3 with control (n = 3 mice) or *shCbln4*-expressing virus (n = 3 mice) and analyzed in the somatosensory cortex at P27. No significant differences, Student t-test. *Right:* quantification of mCherry+Syt2+ boutons inside the mCherry+ axons of sparsely labeled PV+ cells contacting Gephyrin+ postsynaptic clusters in the lower layers of the prefrontal cortex of *Nkx2-1^{CreER/+}* mice induced with Tamoxifen and infected at P2 with control (n = 9 cells from 4 mice) or *shCbln4*-expressing virus (n = 6 cells from 3 mice) and analyzed at P25. No significant differences, Mann-Whitney test. Note that the use of *Lhx6^{Cre/+}* mice (left bar graph) implies having both PV+ and SST+ cells that are knockdown for *Cbln4*. The use of *Nkx2-1^{CreER/+}* mice (right bar graph) allowed sparse labeling and hence ensured a cell-autonomous effect of the downregulation in PV+ cells only. (**B**) Quantification of mCherry+ synapses per surface unit of axon initial segment (AnkG) made by *Nkx2-1^{CreER/+}* chandelier cells induced with Tamoxifen and infected at P2 with control (n = 8 cells from 2 mice) or *shCbln4*-expressing virus (n = 14 cells from 3 mice) and analyzed at P25. No significant differences, Student t-test. (**C**) Quantification of GAD65+ boutons inside the mCherry+ axons of SST+ cells contacting Gephyrin+ postsynaptic clusters in layer I of the somatosensory cortex of *Lhx6^{Cre/+}* mice injected at P3 with control (n = 6 mice) or *shLgi2*-expressing virus (n = 7 mice) and analyzed at P30. No significant differences, Student t-test. (**D**) Quantification of mCherry+ synapses per surface unit of axon initial segment (AnkG) made by *Nkx2-1^{CreER/+}* chandelier cells induced with Tamoxifen and infected at P2 with control (n = 9 cells from 3 mice) or *shLgi2*-expressing virus (n = 8 cells from 3 mice) and analyzed at P25. No significant differences, Student t-test. (**E**) Quantification of GAD65+ boutons inside the mCherry+ axons of SST+ cells contacting Gephyrin+ postsynaptic clusters in layer I of the somatosensory cortex of *Lhx6^{Cre/+}* mice injected at P3 with control (n = 3 mice) or *shFgf13*-expressing virus (n = 3 mice) and analyzed at P27. No significant differences, Student t-test. (**F**) Quantification of mCherry+Syt2+ somatic synapses per surface unit of pyramidal cell soma in *PV^{Cre/+}* mice injected at P3 with control (n = 4 mice) or *shFgf13*-expressing virus (n = 3 mice) and analyzed at P30. No significant differences, Mann-Whitney test.

A

SST+ cells /mm²

L2/3   L4   L5   L6

□ *shControl*
□ *shCbln4*

B

PV+ cells /mm²

L2/3   L4   L5   L6

□ *shControl*
□ *shLgi2*

C

ns

ChCs+ cells /mm²
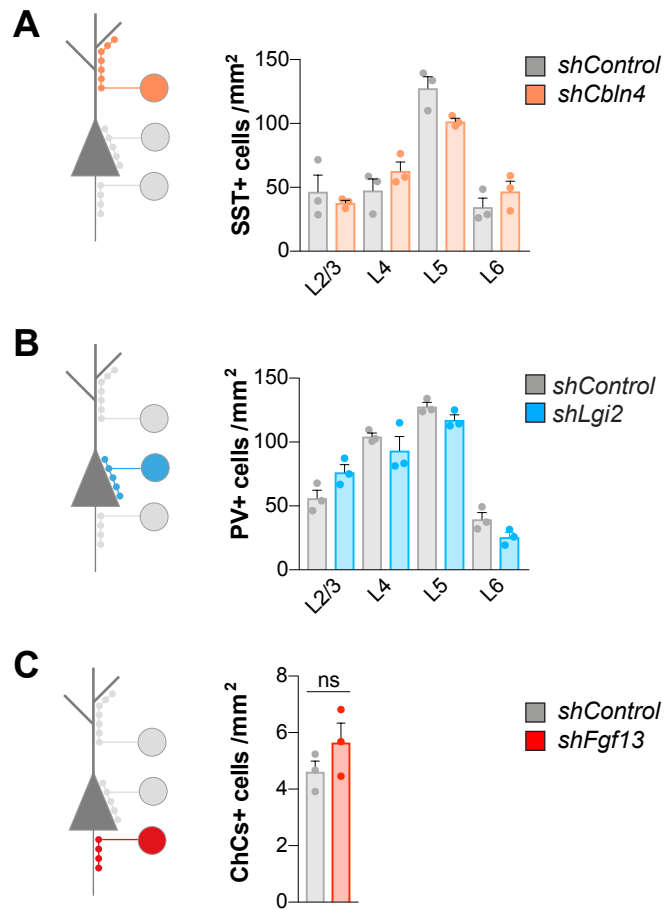
□ *shControl*
□ *shFgf13*

Figure S18

Fig. S18. The number and distribution of interneurons is not affected by the absence of *Cbln4*, *Lgi2* or *Fgf13*.

(**A**) Number and distribution of SST+ cells in the mouse somatosensory cortex of *SST-Cre* mice injected at P3 with control (n = 3 mice) or *shCbln4*-expressing virus (n = 3 mice) and analyzed at P30. Two-way ANOVA, control vs *shCbln4*: p = 0.1789, layer effect: p = <0.0001, interaction: p = 0.1105. No significant differences were detected by Sidak's multiple comparisons test between control and *shCbln4*. Note that analysis was performed in slices where 100% of SST+ cells were infected. (**B**) Number and distribution of PV+ cells in the mouse somatosensory cortex of *Lhx6*$^{Cre/+}$ mice injected at P3 with control (n = 3 mice) or *shLgi2*-expressing virus (n = 3 mice) and analyzed at P30. Two-way ANOVA, control vs *shLgi2*: p = 0.3699, layer effect: p = <0.0001, interaction: p = 0.1291. Note that analysis was performed in slices where 100% of PV+ cells were infected. (**C**) Number of mCherry+ chandelier cells (normalized by the total number of PV+ cells infected by each virus) in the upper layers of the mouse prefrontal cortex of *Nkx2-1*$^{CreER/+}$ mice induced with Tamoxifen and infected at P2 with control (n = 3 mice) or *shFgf13*-expressing virus (n = 3 mice) and analyzed at P30. No significant differences, Student t-test.
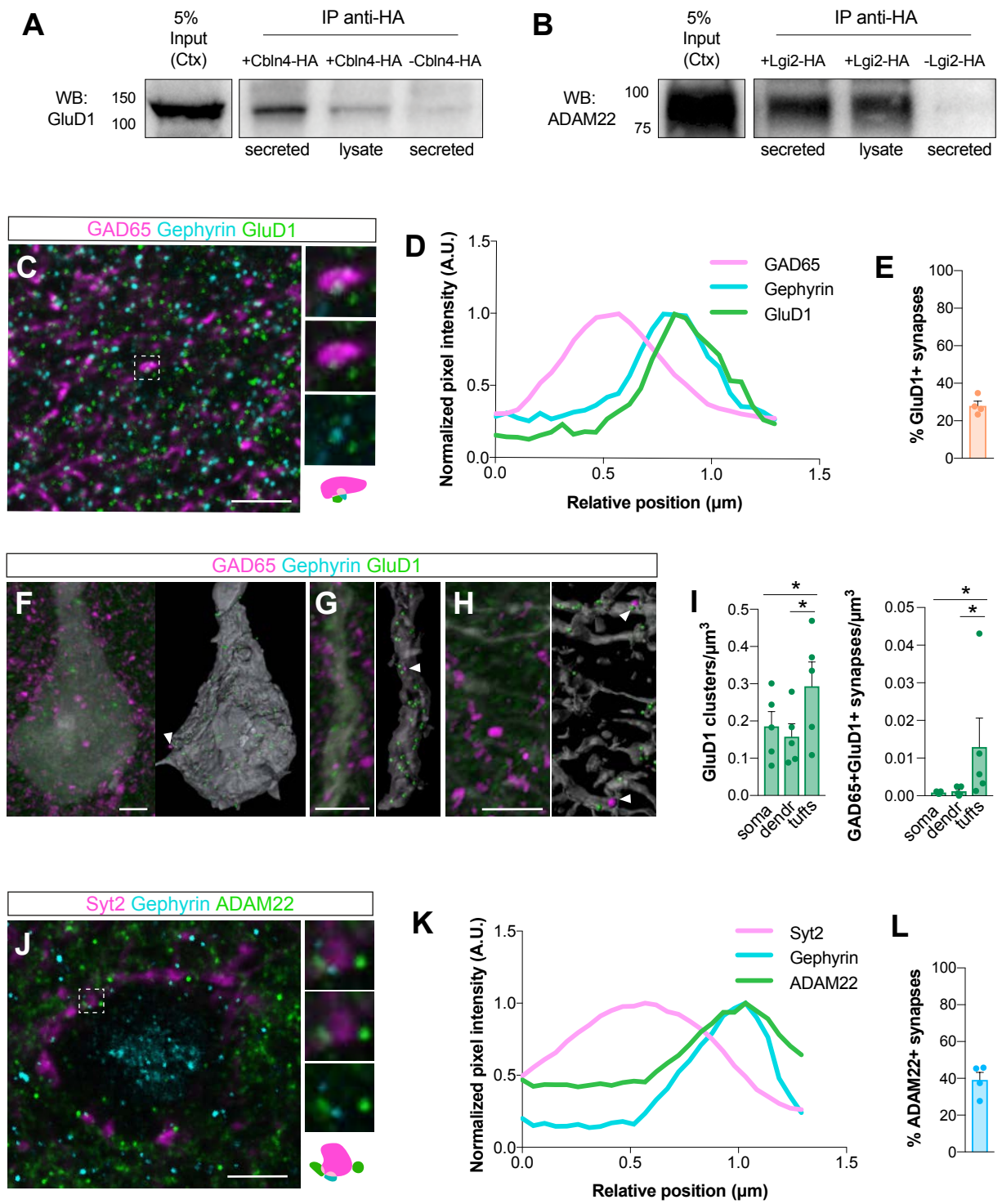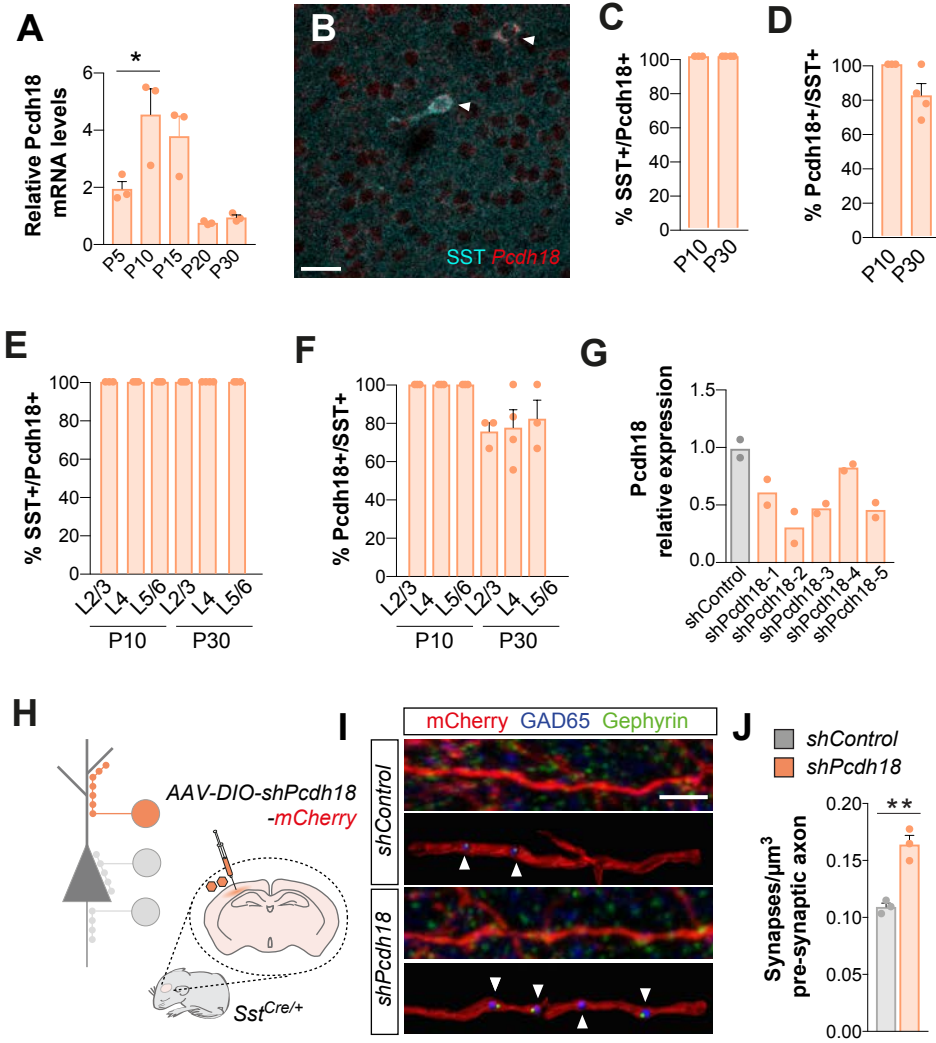
Figure S19

Fig. S19. Characterization of CBLN4 and LGI2 trans-synaptic partners GluD1 and ADAM22.

(**A-B**) Representative immunoblot illustrating that pull-down of Cbln4-HA and Lgi2-HA co-immunoprecipitates (IP), respectively, GluD1 (A) and ADAM22 (B) from wild type P30 cortical lysates (n = 5 experiments, 80% and 40% co-IP success rate for GluD1 and ADAM22, respectively). (**C-D**) Representative image (C) and profile plot (D) showing the localization of GluD1 at the GAD65+Gephyrin+ synapses made by SST+ cells in layer I of P30 mouse somatosensory cortex (n = 30 synapses from 3 mice). (**E**) Percentage of GAD65+Gephyrin+ synapses that colocalize with GluD1 at P30 in layer I of the mouse somatosensory cortex (n = 3 mice). (**F-I**) Representative images, imaris reconstructions (F-I) and density (I) of GluD1+ clusters as well as GAD65+GluD1+ synapses on the dendritic tufts (where the majority of SST+ synapses are made) versus distal dendrites or somata of pyramidal cells labeled at P3 with injection of a GFP-expressing virus and analyzed at P30 (n = 5 mice). *$p<0.05$, Kruskal-Wallis test followed by Dunn's multiple comparisons test. (**J-K**) Representative image (J) and profile plot (K) showing the localization of ADAM22 at the Syt2+Gephyrin+ synapses made by PV+ cells around the soma of pyramidal neurons at P30 (n = 30 synapses from 3 mice). (**L**) Percentage of Syt2+Gephyrin+ that colocalize with ADAM22 at P30 in the mouse somatosensory cortex (n = 3 mice). Scale bars equal 4 μm.

A Relative Pcdh18 mRNA levels — P5, P10, P15, P20, P30; *

B SST *Pcdh18*

C % SST+/Pcdh18+ — P10, P30

D % Pcdh18+/SST+ — P10, P30

E % SST+/Pcdh18+ — L2/3, L4, L5/6 (P10), L2/3, L4, L5/6 (P30)

F % Pcdh18+/SST+ — L2/3, L4, L5/6 (P10), L2/3, L4, L5/6 (P30)

G Pcdh18 relative expression — shControl, shPcdh18-1, shPcdh18-2, shPcdh18-3, shPcdh18-4, shPcdh18-5

H AAV-DIO-shPcdh18-mCherry; Sst$^{Cre/+}$

I mCherry GAD65 Gephyrin — *shControl*, *shPcdh18*

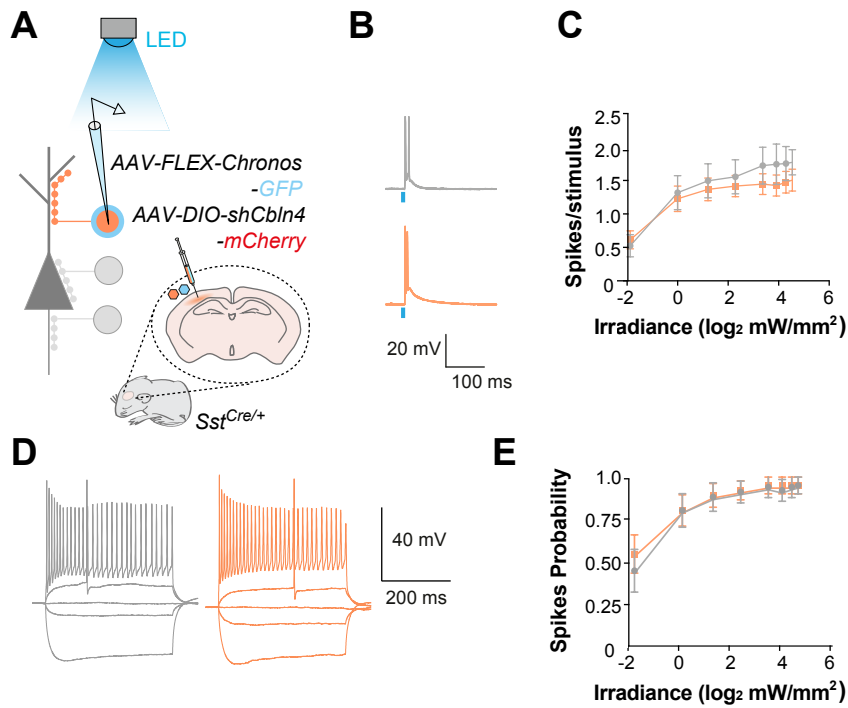**J** Synapses/µm^3 pre-synaptic axon — *shControl*, *shPcdh18*; **

Figure S20

Fig. S20. *Pcdh18* **is specifically expressed in SST+ cells and regulates the development of SST+ synapses.**

(**A**) Developmental expression of *Pcdh18* in the mouse somatosensory cortex assessed by qPCR as expression relative to *18S* (n = 3 mice for each stage). *p<0.05 for P5 vs P10, P15 vs P20 and P15 vs P30; **p<0.01 for P10 vs P20 and P10 vs P30; One-Way ANOVA followed by Tukey's multiple comparisons test. Note that significance is shown only for the P5-P10 comparison. (**B**) Representative image showing the colocalization of *Pcdh18* mRNA with SST+ cells. Scale bar equal to 20 μm. (**C**) Quantification of the specificity of *Pcdh18* expression in SST+ interneurons subpopulations at P10 and P30 (n ≥ 3 mice for each stage). (**D**) Fraction of SST+ cells that express *Pcdh18* at P10 and P30 (n ≥ 3 mice for each stage). (**E**) Percentage of *Pcdh18*+ cells (detected by in situ hybridization) that express SST in the indicated layers of the mouse somatosensory cortex at P10 and P30 (n ≥ 3 mice for each stage). (**F**) Percentage of SST+ cells that express *Pcdh18* in the indicated layers of the mouse somatosensory cortex at P10 and P30 (n ≥ 3 mice for each stage). (**G**) *Pcdh18* mRNA expression (relative to 18S) assessed by qPCR (and shown as expression relative to control) upon co-transfection of HEK cells with an HA-tagged *Pcdh18* expression plasmid and corresponding shRNAs (n = 2 experiments. (**H**) Schematic of AAV injections in the somatosensory cortex of *SST*-Cre mice. (**I-J**) Representative image, Imaris reconstruction (**I**) and quantification (**J**) of GAD65+ boutons inside the mCherry+ axons of SST+ cells contacting Gephyrin+ postsynaptic clusters in layer I of the somatosensory cortex of *SST-Cre* mice injected at P3 with control (n = 3 mice) or *shPcdh18*-expressing virus (n = 3 mice) and analyzed at P30. **p<0.01, Student t-test. Scale bar equal 3 μm.

A LED
AAV-FLEX-Chronos
-*GFP*
AAV-DIO-shCbln4
-*mCherry*
Sst^Cre/+

B
20 mV
100 ms

C

D
40 mV
200 ms

E

F

Feature	shLacZ			shCbln4			*p*	Significance	Statistical Comparison
	Mean	Std. Err.	n	Mean	Std. Err.	n			
AP Threshold (mV)	-44.4	0.9	16	-45.2	1.3	20	0.627	ns	t-test
Delay to first AP (ms)	126.0	19.6	16	145.0	20.5	20	0.519	ns	t-test
AP amplitude (mv)	67.3	2.3	16	73.1	2.3	20	0.114	ns	Mann-Whitney
AP half-width (ms)	1.1	0.1	16	1.1	0.1	20	0.826	ns	t-test
Fast AHP amplitude (mV)	13.4	1.5	16	11.5	1.3	20	0.323	ns	t-test
Fast AHP timing (ms)	3.8	0.3	16	3.7	0.3	20	0.587	ns	Mann-Whitney
Rheobase (pA)	54.6	11.9	16	74.1	10.4	20	0.118	ns	Mann-Whitney
Maximum Firing Frequency (Hz)	75.6	10.0	16	87.3	9.0	20	0.393	ns	t-test
Adaptation Ratio (%)	-45.2	6.5	16	-41.9	4.0	20	0.832	ns	Mann-Whitney
Input Resistance (MΩ)	247.0	30.4	16	197.0	20.0	20	0.162	ns	t-test
Voltage Sag at -100 mV (mV)	-4.2	0.8	16	-4.6	0.8	20	0.686	ns	t-test
Tau (ms)	13.6	1.9	15	13.0	1.4	19	0.945	ns	Mann-Whitney
Capacitance (pF)	52.4	3.0	15	66.1	4.6	19	0.019	*	Mann-Whitney
Resting Membrane Potential (mV)	-63.1	1.2	16	-64.9	0.8	20	0.118	ns	Mann-Whitney

Abbreviations AP: Action Potential; AHP: After-hyperpolarisation; ns: not significant

Figure S21

Fig. S21. Functional reduction in SST dendritic inhibition upon loss of function of *Cbln4*.

(**A**) Schematic of AAV injections in the indicated regions and Cre-expressing mice and optogenetic activation. (**B**) Example responses to current steps delivered for intrinsic property analysis for SST interneurons in the somatosensory cortex of *SST-Cre* mice injected at P3 with control or *shCbln4*-expressing virus. (**C**) Number of spikes elicited per optogenetic stimulus as a function of irradiance (control, n = 16 cells; s*hCbln4* n = 19 cells), ns, Two-Way ANOVA. (**D**) Intrinsic properties for SST interneurons recorded from control or *shCbln4*-injected mice. (**E**) Spike probability as a function of irradiance (control, n = 16 cells; *shCbln4* n = 19 cells), ns, Two-Way ANOVA. (**F**) Intrinsic properties for SST interneurons recorded from mice injected with control or shCbln4-virus.
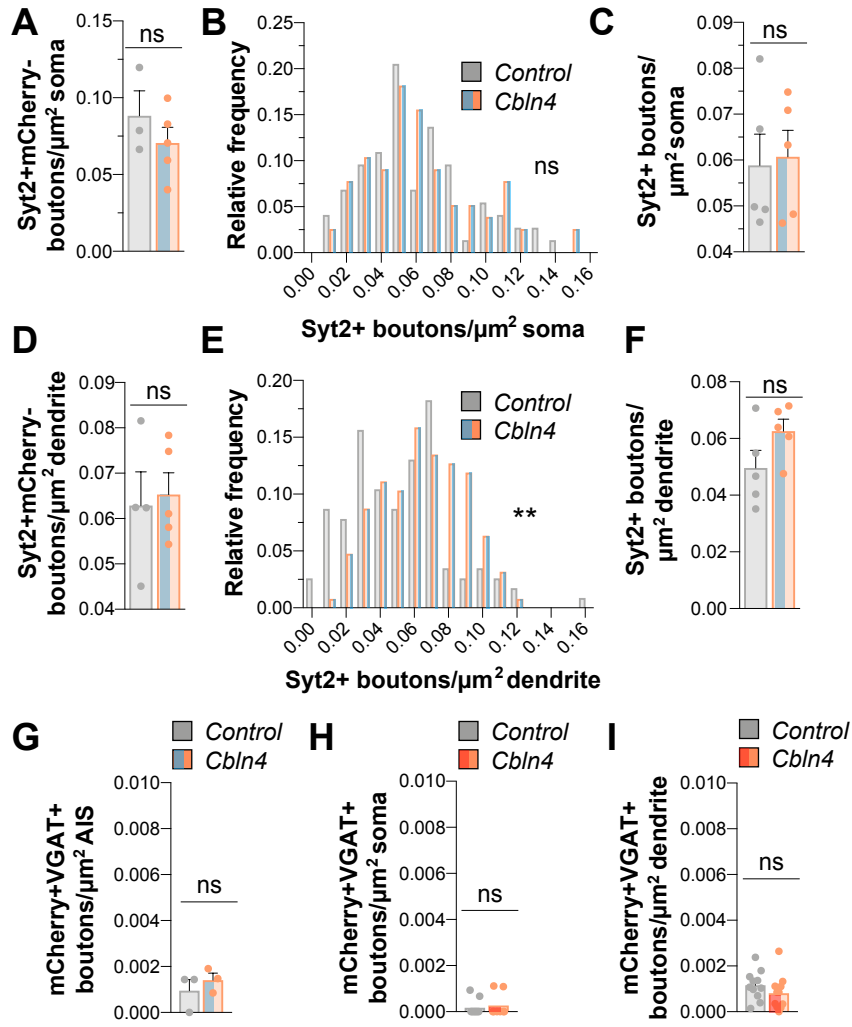
Figure S22

Fig. S22. Overexpression of CBLN4 in PV+ and chandelier cells alters their synapses in a domain-specific manner.

(**A**) Quantification of mCherry-Syt2+ somatic synapses per surface unit of pyramidal cell soma in $PV^{Cre/+}$ mice injected at P3 with control (n = 5 mice) or $Cbln4$-HA-expressing virus (n = 5 mice). ns, Student t-test. (**B**) Relative frequency distribution of Syt2+ presynaptic boutons per surface unit of pyramidal cell soma in $PV^{Cre/+}$ mice injected at P3 with control (n = 5 mice) or $Cbln4$-HA-expressing virus (n = 5 mice). ns, Kolmogorov-Smirnov test. (**C**) Quantification of Syt2+ presynaptic boutons per surface unit of pyramidal cell soma in $Lhx6^{Cre/+}$ mice injected at P3 with control (n = 5 mice) or $Cbln4$-HA-expressing virus (n = 5 mice). ns, Student t-test. (**D**) Quantification of mCherry-Syt2+ somatic synapses per surface unit of pyramidal cell dendrite in $PV^{Cre/+}$ mice injected at P3 with control (n = 5 mice) or $Cbln4$-HA-expressing virus (n = 5 mice). ns, Student t-test. (**E**) Relative frequency distribution of Syt2+ presynaptic boutons per surface unit of pyramidal cell dendrite in $PV^{Cre/+}e$ mice injected at P3 with control (n = 5 mice) or $Cbln4$-HA-expressing virus (n = 5 mice). **$p<0.01$, Kolmogorov-Smirnov test. (**F**) Quantification of Syt2+ presynaptic boutons per surface unit of pyramidal cell dendrite in $PV^{Cre/+}$ mice injected at P3 with control (n = 5 mice) or $Cbln4$-HA-expressing virus (n = 5 mice). ns, Student t-test. (**G**) Quantification of mCherry+VGAT+ axo-axonic synapses per surface unit of axon initial segment (AIS) in $PV^{Cre/+}$ mice injected at P3 with control (n = 3 mice) or $Cbln4$-HA-expressing virus (n = 3 mice). ns, Mann Whitney test. Note that, excluding cartridges from chandelier cells, PV+ cells make virtually no axo-axonic synapse. Because Syt2 is found only at PV+ somatic synapses, VGAT was used here on the assumption that PV+ ectopic synapses onto the AIS may lose Syt2. (**H**) Quantification of mCherry+ synapses per surface unit of pyramidal cell soma made by $Nkx2$-$1^{CreER/+}$ chandelier cells induced with Tamoxifen at P2 and infected with control (n = 9 cells from 3 mice) or $Cbln4$-HA-expressing virus (n = 8 cells from 3 mice). ns, Mann Whitney test. (**I**) Quantification of mCherry+ synapses per surface unit of pyramidal cell dendrite made by $Nkx2$-$1^{CreER/+}$ chandelier cells induced with Tamoxifen at P2 and infected with control (n = 11 cells from 3 mice) or $Cbln4$-HA-expressing virus (n = 11 cells from 3 mice). ns, Mann Whitney test.

Mouse strain	Type of synapses	Cell	T1	T2	Brain region	Replicates
Nkx2.1CreERT2; Ai9	AIS-targeting	Chandelier cells	P8	P10	PFC, upper layers	3
G42	Soma-targeting	PV+ basket cells	P5	P10	PFC, lower layers	3
GIN	Dendrite-targeting	Martinotti cells	P5	P10	SSC, all layers	3
Nex-Cre;RCE	Glutamatergic synapses	Pyramidal cells	NA	P12	PFC, all layers	3
Nkx2.1Cre;RCE	General interneuron genes	Interneurons	P0	NA	PFC, all layers	3
PLP-GFP	General oligodendrocyte genes	Oligodendrocytes	NA	P10	PFC, upper layers	2

Table S1

Table S1. **Transgenic lines, brain regions and stages used for gene expression profiling.**

Table S2. RNA integrity numbers for all samples

	RIN
SST_P10	9.2
SST_P10	8.2
SST_P10	8.8
SST_P5	9.3
SST_P5	7.4
SST_P5	9.9
PVBC_P10	8.9
PVBC_P10	7.7
PVBC_P10	6.9
PVBC_P5	9.3
PVBC_P5	7.2
PVBC_P5	8.9
ChC_P10	9.5
ChC_P10	8.7
ChC_P10	9.7
ChC_P8	9.6
ChC_P8	7.6
ChC_P8	6.3
PYR_P12	10
PYR_P12	9.3
PYR_P12	10
IN_P0	6.5
IN_P0	7.7
IN_P0	8.9
OLIG_P10	9.9
OLIG_P10	9.6

Table S2. **RNA integrity numbers for the samples used in the RNAseq experiment.**

Table S3. **Gene expression and specificity of all transcripts from the isolated cell populations.** Table provided as separate file.

Table S4. **Matching interneuron subtype-specific and pyramidal cell gene/protein-pairs.** Table provided as separate file.

References (*31, 59*)

31.   S. Hippenmeyer *et al.*, A developmental switch in the response of DRG neurons to ETS transcription factor signaling. *PLoS Biol*. **3**, e159 (2005).

32.   N. Spassky *et al.*, The early steps of oligodendrogenesis: insights from the study of the plp lineage in the brain of chicks and rodents. *Dev Neurosci*. **23**, 318–326 (2001).

33.   Q. Xu, M. Tam, S. A. Anderson, Fate mapping Nkx2.1-lineage cells in the mouse telencephalon. *J Comp Neurol*. **506**, 16–29 (2008).

34.   S. Goebbels *et al.*, Genetic targeting of principal neurons in neocortex and hippocampus of NEX-Cre mice. *Genesis*. **44**, 611–621 (2006).

35.   T. Miyamae, K. Chen, D. A. Lewis, G. Gonzalez-Burgos, Distinct Physiological Maturation of Parvalbumin-Positive Neuron Subtypes in Mouse Prefrontal Cortex. *J Neurosci*. **37**, 4883–4902 (2017).

36.   D. M. Gelman, O. Marín, Generation of interneuron diversity in the mouse cerebral cortex. *Eur J Neurosci*. **31**, 2136–2141 (2010).

37.   A. J. Hinojosa, R. Deogracias, B. Rico, The microtubule regulator NEK7 coordinates the wiring of cortical parvalbumin interneurons. *Cell Rep*. **24**, 1231–1242 (2018).

38.   Y. Ma, H. Hu, A. S. Berrebi, P. H. Mathers, A. Agmon, Distinct subtypes of somatostatin-containing neocortical interneurons revealed in transgenic mice. *J Neurosci*. **26**, 5069–5082 (2006).

39.   B. Halabisky, F. Shen, J. R. Huguenard, D. A. Prince, Electrophysiological classification of somatostatin-positive interneurons in mouse sensorimotor cortex. *J Neurophysiol*. **96**, 834–845 (2006).

40.   B. Tasic *et al.*, Shared and distinct transcriptomic cell types across neocortical areas. *Nature*. **563**, 72–78 (2018).

41.   B. B. Babraham Bioinformatics, Babraham Bioinformatics - FastQC A Quality Control tool for High Throughput Sequence Data, (available at http://www.bioinformatics.babraham.ac.uk/projects/fastqc/).

42.   R. Schmieder, Y. W. Lim, R. Edwards, Identification and removal of ribosomal RNA sequences from metatranscriptomes. *Bioinformatics*. **28**, 433–435 (2012).

43.   D. Kim *et al.*, TopHat2: accurate alignment of transcriptomes in the presence of insertions, deletions and gene fusions. *Genome Biol*. **14**, R36 (2013).

44.   C. Trapnell *et al.*, Transcript assembly and quantification by RNA-Seq reveals unannotated transcripts and isoform switching during cell differentiation. *Nat Biotechnol*. **28**, 511–515 (2010).

45.   C. Trapnell *et al.*, Differential analysis of gene regulation at transcript resolution with RNA-seq. *Nat Biotechnol*. **31**, 46–53 (2013).

46.   C. Trapnell *et al.*, Differential gene and transcript expression analysis of RNA-seq experiments with TopHat and Cufflinks. *Nat Protoc*. **7**, 562–578 (2012).

47.   C. Stark *et al.*, BioGRID: a general repository for interaction datasets. *Nucleic Acids Res*. **34**, D535-9 (2006).

48.   D. Szklarczyk *et al.*, The STRING database in 2017: quality-controlled protein-protein association networks, made broadly accessible. *Nucleic Acids Res*. **45**, D362–D368 (2017).

49.   M. N. Cabili *et al.*, Integrative annotation of human large intergenic noncoding RNAs reveals global properties and specific subclasses. *Genes Dev*. **25**, 1915–1927 (2011).

50.   G. Miyoshi *et al.*, Prox1 Regulates the Subtype-Specific Development of Caudal Ganglionic Eminence-Derived GABAergic Cortical Interneurons. *J Neurosci*. **35**, 12869–12889 (2015).

51.   S. Gu *et al.*, The loop position of shRNAs and pre-miRNAs is critical for the accuracy of dicer processing in vivo. *Cell*. **151**, 900–911 (2012).

52.   N. Spruston, Pyramidal neurons: dendritic structure and synaptic integration. *Nat Rev Neurosci*. **9**, 206–221 (2008).

53.   P. Fazzari *et al.*, Control of cortical GABA circuitry development by Nrg1 and ErbB4 signalling. *Nature*. **464**, 1376–1380 (2010).

54.   M. Inan *et al.*, Dense and overlapping innervation of pyramidal neurons by chandelier cells. *J Neurosci*. **33**, 1907–1914 (2013).

55.   Y. Tai, J. A. Janas, C.-L. Wang, L. Van Aelst, Regulation of chandelier cell cartridge and bouton development via DOCK7-mediated ErbB4 activation. *Cell Rep*. **6**, 254–263 (2014).

56.   L. Lim *et al.*, Optimization of interneuron function by direct coupling of cell migration and axonal targeting. *Nat Neurosci*. **21**, 920–931 (2018).

57.   J. T. Ting, T. L. Daigle, Q. Chen, G. Feng, Acute brain slice methods for adult and aging animals: application of targeted patch clamp analysis and optogenetics. *Methods Mol Biol*. **1183**, 221–242 (2014).

58.   P. G. Anastasiades, A. Marques-Smith, S. J. B. Butt, Studies of cortical connectivity using optical circuit mapping methods. *J Physiol (Lond)*. **596**, 145–162 (2018).

59.   T. J. Viney *et al.*, Network state-dependent inhibition of identified hippocampal CA3 axo-axonic cells in vivo. *Nat Neurosci*. **16**, 1802–1811 (2013).